Sec18 side-loading is essential for universal SNARE recycling across cellular contexts

Yousuf A. Khan[1,2,3,4,9], K. Ian White[1,2,3,4,5], Richard A. Pfuetzner[1,2,3,4,5], Bharti Singal[6], Luis Esquivies[1,2,3,4,5], Garvey Mckenzie[7], Fang Liu[7], Katherine DeLong[1], Uchoer B. Choi[1,2,3,4,5], Elizabeth Montabana[6], Theresa Mclaughlin[7], William T. Wickner[8], Axel T. Brunger[1,2,3,4,5,9*]

[1]Department of Molecular and Cellular Physiology, Stanford University, Stanford, CA, USA
[2]Department of Neurology and Neurological Sciences, Stanford University, Stanford, CA, USA
[3]Department of Structural Biology, Stanford University, Stanford, CA, USA
[4]Department of Photon Science, Stanford University, Stanford, CA, USA
[5]Howard Hughes Medical Institute, Stanford University, Stanford, CA, USA
[6]Stanford Cryo-EM microscopy center, Stanford University, Palo Alto, CA, USA
[7]Stanford University Mass Spectrometry, Stanford University, Palo Alto, CA, USA
[8]Department of Biochemistry and Cell Biology, Geisel School of Medicine at Dartmouth, Dartmouth College, Hanover, NH 03755.
[9]Correspondence: yousuf@stanford.edu (YAK), brunger@stanford.edu (ATB)

Summary

SNARE proteins drive membrane fusion as their core domains zipper into a parallel four-helix bundle[1,2]. After fusion, these bundles are disassembled by the AAA+ protein Sec18/NSF and its adaptor Sec17/ α-SNAP[3,4] to make them available for subsequent rounds of membrane fusion. SNARE domains are often flanked by C-terminal transmembrane or N-terminal domains[5]. Previous structures of the NSF–α-SNAP–SNARE complex revealed SNARE domain threaded through the D1 ATPase ring[6], posing a topological constraint as SNARE transmembrane domains would prevent complete substrate threading as suggested for other AAA+ systems[7]. Here, *in vivo* mass-spectrometry reveals N-terminal SNARE domain interactions with Sec18, exacerbating this topological issue. Cryo-EM structures of a yeast SNARE complex, Sec18, and Sec17 in a non-hydrolyzing condition shows SNARE Sso1 threaded through the D1 and D2 ATPase rings of Sec18, with its folded, N-terminal Habc domain interacting with the D2 ring. This domain does not unfold during Sec18/NSF activity. Cryo-EM structures under hydrolyzing conditions revealed substrate-released and substrate-free states of Sec18 with a coordinated opening in the side of the ATPase rings. Thus, Sec18/NSF operates by substrate side-loading and unloading topologically constrained SNARE substrates.

Keywords:

ATPases associated with diverse cellular activities (AAA+);
N-ethylmaleimide-sensitive factor (NSF);
Sec18;
Soluble N-ethylmaleimide sensitive factor Attachment protein Receptor (SNARE);
Exocytosis;
Quality control;
cryo-electron microscopy;
single-molecule fluorescence resonance energy transfer;

Main

Cellular compartmentalization, growth, hormone secretion, transport, neurotransmission, and many other pathways depend on precise, rapid, and regulated membrane fusion[8,9]. Membrane fusion in eukaryotic cells is mediated by a highly conserved superfamily of SNAREs (Soluble N-ethylmaleimide sensitive factor Attachment protein Receptors)[5]. All SNAREs share a characteristic 60–70 amino acid SNARE domain often flanked by a C-terminal transmembrane domain, membrane anchors, and a folded N-terminal variable domain specific to the SNARE's function and intracellular pathway[10]. SNAREs on opposing membranes interact primarily through their SNARE domains to form a parallel *trans*-SNARE complex, juxtaposing two different membranes[11,12]. Membrane fusion commences when these SNARE domains zipper together in a directed fashion[1,2]. After fusion, the SNAREs form a highly stable parallel helical bundle, the so-called *cis*-SNARE complex[1]. This highly stable four-helix *cis*-SNARE complex is disassembled by Sec18 (N-ethylmaleimide-sensitive factor, NSF, in higher eukaryotes)[4,13,14] to provide the energy for subsequent membrane fusion events[15].

Sec18/NSF is a universally conserved AAA+ (ATPases associated with diverse cellular activities) protein translocase[16–18]. Sec18/NSF consists of an N-domain, an active D1 AAA+ domain, and a catalytically inactive D2 AAA+ oligomerization domain[19]. It was initially discovered as a critical complementation group required by the yeast secretory pathway, and it is now known for its role in recycling SNAREs[20] and SNARE assembly quality control for proper SNARE complex assembly[21–24]. Sec18/NSF, with the adaptor protein Sec17 (α-SNAP in higher eukaryotes), disassembles *cis*-SNARE complexes. The disassembly requires multiple ATP hydrolysis events in the presence of Mg^{2+} ; as few as 6 ATP hydrolysis events are sufficient[25,26].

Cryo-EM structures of the mammalian 20S complex (NSF, α-SNAP, and neuronal SNAREs ternary complex) in a non-hydrolyzing condition (*i.e.*, in the absence of divalent cations) revealed a supramolecular architecture in which the NSF N-domains bind α-SNAP molecules, three or four of which in turn bind the four-helix SNARE complex consisting of the SNARE domains of syntaxin-1A, SNAP-25, and synaptobrevin[3,13]. The N-terminal residues of the SNARE domain of SNAP-25 was bound to the D1 ring pore without apparent ATP hydrolysis, where it interacts with several conserved tyrosine amino acids in a spiral staircase-

like pattern[13,16,27]. In these EM maps, no ordered density was observed in the D2 ring pore, consistent with the notion that it is catalytically inactive and primarily responsible for NSF oligomerization rather than substrate engagement[28]. The interaction between the SNARE substrate and the D1 pore is like that observed for other AAA+ translocases and suggests a conserved mechanism for substrate threading through the D1 pore. However, the membrane anchors and domains of the SNAREs would seemingly prevent complete threading of the type suggested for other AAA+ systems[7,29,30], posing a topological challenge. Furthermore, SNAREs contain globular N-terminal domain(s) of variable length and structure; for example, the N-terminal domain of syntaxin consists of a three-helix bundle (Habc domain) involved in regulating its function[31], and the N-terminal domains of Use1 and Sec20 in part form a stable 255 kDa tethering complex[32]. Complete threading would imply that such N-terminal domains are somehow unfolded. These topological constraints surrounding SNARE loading, processing, and release through Sec18/NSF are further compounded by the observation that Sec18/NSF disassembles all SNAREs in all cellular contexts[5,10,33], which all contain a variety of different N- and C-terminal domains and membrane arrangements/linkages.

In vivo **cross-linking mass-spectrometry with Sec18**

These questions led us to investigate the space of Sec18/NSF—SNARE interactions through *in vivo* protein crosslinking mass-spectrometry (XL-MS) in yeast. Due to its power as a model system and relatively simple SNARE proteome, *S. cerevisiae* is an excellent model for investigating Sec18 interactions with different substrates in live cells. As such, we developed a protocol for *in vivo* crosslinking mass-spectrometry (XL-MS) in yeast to identify binding partners of Sec18 (**Extended Data Figure 1A, Methods**).

In total, 35 identified proteins are shared between disuccinimidyl glutarate crosslinker (DSG) treated and untreated conditions (*i.e.*, they are non-specific proteins) (**Figure 1A**). The nine proteins observed only in the untreated condition had few unique spectra mapping to their identified proteins, suggesting that they were not detected in the treated condition due to their low abundance and difficulty of consistent detection. The 205 proteins unique to the 5 mM DSG treated condition were processed using spatial analysis of functional enrichment (SAFE) analysis to visualize the various cellular processes to which the identified proteins contribute[34]. At increasing levels of significance thresholds (p = 0.01, 0.001, and 0.0001), the identified proteins only enriched the vesicle trafficking processes. Gene ontology (GO) analysis also revealed lesser-known processes, such as vacuolar acidification and ergosterol biosynthesis (**Supplementary Figure 1**), consistent with Sec18's functions in these contexts[35–37]. The enrichment of these processes validated our crosslinking protocol for specifically targeting Sec18 and its binding partners inside the cell.

Within our enriched protein dataset, we found many yeast SNAREs involved in different pathways and compartments of the cell. We then mapped crosslinked residues of these SNAREs to those of Sec18 (**Figure 1B**). Using a series of empirical constraints (**Methods**), we classified a crosslink as high confidence if it met all constraints, medium confidence if it met some but not all, and low confidence if it did not. Since crosslinking was performed in live cells, we expect

these crosslinks to represent interactions between SNAREs and Sec18 during substrate loading, disassembly, and substrate release.

Previous cryo-EM structures of the complex of NSF, α-SNAP, and neuronal SNAREs in a non-hydrolyzing condition revealed that the four-helix SNARE bundle interacts with between two and four α-SNAP molecules, which in turn are bound by the N-domains of NSF; the N-terminal end of one of the SNAREs is bound to the pore of the D1 ring[3,13,27]. Consistent with these structures, we found crosslinks between SNARE domains and the N-domain or D1 domain (examples in **Figure 1C, E, F**). Additionally, we observed several high-confidence crosslinks of yeast SNARE proteins to the D2 domain, an unexpected result given an absence of interactions between the SNAREs and the D2 ring in the cryo-EM structures and that the D2 domain is catalytically inactive[19] and has had no previously reported role in SNARE recycling. Considering this unexpected result, we thus focused on SNAREs with at least one high-confidence crosslink to the D2 domain of Sec18 (**Figures 1C-F**).

Specifically, seven of ten high-confidence D2 crosslinks connect to regions N-terminal to a SNARE domain (**Figures 1C-F**). For example, for Sso1, the high-confidence crosslink to D2 involves its Habc domain (**Figure 1D, Extended Data Figure 1B**). The Habc domain is a stable three-helix bundle[31]; thus, assuming complete threading through the D1 and D2 pores, the Habc domain (~30 Å diameter) would have to be unfolded transiently. The remaining three high-confidence D2 crosslinks connect to C-terminal regions within SNARE domains. At first glance, this suggests complete substrate threading through both the D1 and D2 rings, akin to other AAA+ protein translocases[38]. However, considering the topology imposed by membrane domains, anchors, and folded N-terminal domains, how is a SNARE substrate loaded and released? To answer these vexing topological questions, we next determined cryo-EM structures of this orthologous yeast complex together with Sec18 and Sec17.

The Sec18—Sec17—Sso1—Snc1—Sec9 (y20S) complex

To corroborate the surprising LC-MS/MS results, we determined cryo-EM structures of a yeast SNARE complex together with Sec18 and Sec17. We chose the Sso1—Sec9 —Snc1/Snc2 complex (referred to as ySNARE complex) since each component of this complex crosslinked with high confidence to the D2 domain of Sec18 (Snc1 is highly homologous to Snc2). We prepared the Sec18—Sec17—Sso1—Snc1—Sec9 (y20S) complex (**Extended Data Figure 2, Methods**), and after single particle cryo-EM data collection and processing, we obtained 381,591 high-quality particles that yielded eight 3D classes into which models were built (**Figure 2A–E, Supplementary Figure 2A-B, Supplementary Table 1**).

In the structures of all eight classes, Sso1 is threaded through the D1 pore of Sec18 (**Figure 2A**). A characteristic phenylalanine side chain density in Sso1 is present at the same position relative to Sec18 in all classes, allowing for reliable indexing of Sso1. The nucleotide states and the arrangements of D1 around the substrate were also the same among all eight classes, with the ADP-engaged E protomer forming the top of a spiral staircase of tyrosine residues. Protomers D, B, and C were all ATP bound and formed the middle of the staircase. The

155 bottom protomer, A, forms the base of the staircase. Protomer F, with no apparent density for
156 nucleotide in D1, was not associated with Sso1 (**Figure 2B**). This arrangement of the protomers
157 is driven, in part, by the angle between the more mobile D1 domain and rigid D2 domain. From
158 protomers E to A, the angle between the D1 and D2 decreases monotonically (**Figure 2C**). The
159 protomer at the top of the staircase maintains the largest angle between D1 and D2, while the one
160 at the bottom has the smallest. The eight classes from the non-hydrolyzing y20S dataset also
161 show differences in the ySNARE-Sec17-Sec18-N-domain subcomplex arrangement ("spire")
162 and Sec17 stoichiometry above the D1 ring of the y20S complex before disassembly (**Figure**
163 **2D-E, Extended Data Figure 3B-C**; **Supplementary Discussion**).
164 The high-confidence crosslinks for Sec18 intra- and inter-protomer interactions are
165 consistent with the cryo-EM structure, specifically with the arrangements of the N-domain and
166 D2-domain (**Figure 3A, Extended Data Figure 3A**). Moreover, inter-protomer crosslinks were
167 found between pore loop regions, and between the inter-protomer loop between residues 476 and
168 490 and N-domain linker regions of D1. These high-confidence crosslinks were within the
169 theoretical maximum crosslinking distance (N_ζ–N_ζ: ~40 Å)[39].
170 Remarkably, the structures reveal that Sso1 is also threaded through the D2 pore and that
171 the Habc domain of Sso1 interacts with the outside of the D2 ring, with class 1 having the most
172 well-defined, discrete density (**Figure 3A–E)**. In class 1, the density for Sso1 within Sec18 is
173 continuous from the D1 pore entrance to the D2 pore exit, where the Habc domain begins
174 (**Figure 3A, D**). The three-helix bundle of the Habc domain is then positioned outside the D2
175 pore, where it packs between two small D2 subdomains (protomers A and B) in an interaction
176 driven by charge complementarity. Indeed, the electrostatic potential surface of the Habc domain
177 forms a roughly opposite that of the bottom of the D2 surface against which it packs (**Figure 3B-**
178 **C**). Given that this charge distribution is replicated between each pair of D2 subdomains around
179 the D2 surface, it is unsurprising that the Habc domain adopts multiple corresponding rotational
180 states over the eight classes, presumably due to the flexible linker that follows it (**Figure 3E**).
181 This structural observation is consistent with XL-MS data showing a crosslink between the Habc
182 and the D2 domain of Sec18 (**Figure 3A, Extended Data Figure 1B**). Although the putative
183 distance between the crosslinked residues (K570 in Sec18 and K111 of Sso1) observed in the
184 model for class 1 (42 Å) is at the limit for a crosslinking distance, the conformational flexibility
185 of the Habc domain to rotate and exist in multiple conformations about the D2 ring (**Figure 3E**)
186 likely produces conformations well within the crosslinking distance threshold.
187

188 **Sec18 does not unfold the Sso1/syntaxin Habc domain**

189 Given that this complex was assembled in non-hydrolyzing conditions, we next asked
190 how Sso1 is loaded into Sec18 given the diameter of the Habc domain of Sso1 is ~30 Å whereas
191 the D1 pore of Sec18 has a diameter of ~11 Å. In other AAA+ translocases, such as ClpX, ATP
192 hydrolysis drives complete substrate threading through the AAA+ pore[7]. However, in the case of

193 Sec18 in a non-hydrolyzing condition, such complete threading would require the Habc domain
194 to unfold without any energetic input from Sec18.
195 We employed two orthogonal approaches to test if the Sso1 Habc domain unfolds during
196 SNARE disassembly. In our first approach, we turned to a single-molecule Fluorescence
197 Resonance Energy Transfer (smFRET) system developed previously for NSF, α-SNAP, and
198 neuronal SNAREs[14] in which individual SNARE domains were synthetically linked and
199 stochastically labeled with FRET pairs. This system allows one to observe multiple rounds of
200 SNARE disassembly as the disassembled SNARE domains readily reassemble into a *cis*-SNARE
201 complex due to the covalent linkages. We chose this system since it is well-established.
202 Moreover, it is relevant for the Sec18 system studied here since the primary sequence is
203 conserved in the core regions of Sec18/NSF responsible for ATP hydrolysis and substrate
204 processing (**Extended Data Figure 4A**). In addition, the D1 and D2 rings are structurally
205 conserved when comparing the D1 and D2 rings of Sec18/NSF with engaged substrates, with an
206 average Cα RMSD of 1.64 Å (**Extended Data Figure 4B-C**). The only protomer that exhibits
207 much difference is the F protomer, which is likely due to its mobility and not due to inherent
208 differences between the structures. Furthermore, we tested the ability of Sec18 and Sec17 to
209 disassemble fluorophore-labeled neuronal SNARE and, *vice versa*, NSF and α-SNAP to
210 disassemble fluorophore-labeled exocytic ySNARE complex (**Extended Data Figure 5A-E,**
211 **Supplementary Discussion**). We found that both could process the species-ortholog SNARE
212 complex, albeit at different rates, further corroborating the interchangeability of NSF and Sec18.
213 We thus used the smFRET assay to study the effect of NSF on the dynamics of the three-
214 helix bundle Habc domain of syntaxin during disassembly. We either stochastically labeled the
215 SNARE domains or stochastically labeled the Habc domain at two distinct residue positions to
216 monitor either SNARE disassembly or the folded state of the Habc domain (**Figure 4A**). As in
217 our previous work[14], we observed repeated rounds of disassembly and re-assembly for the
218 SNARE domains as indicated by the changes in single FRET intensity over tens of seconds
219 (**Figure 4B-C**). In stark contrast, we did not observe a change in single-molecule FRET intensity
220 for the labeled Habc domain in non-disassembly and disassembly conditions, producing a FRET
221 intensity distribution consisting only of a high-FRET state (the small peak at 0 is due to traces
222 where acceptor photobleaching occurred since the particular traces never transitioned back to
223 high FRET and no change in the peak intensity between non-disassembly and disassembly
224 conditions was observed) (**Figure 4D-F**). This result suggests that the Habc domain does not
225 unfold during NSF activity.
226 To corroborate this finding with an orthogonal approach for the yeast system, we double-
227 crosslinked the Habc domain of Sso1 by incorporating an unnatural amino acid, 4-azido-L-
228 phenylalanine[40] (**Extended Data Figure 5F-G**). This double crosslink was introduced to prevent
229 the Habc domain from unfolding during any Sec18-driven threading. After crosslinking, we
230 performed a disassembly assay on fluorescently labeled un-crosslinked and crosslinked
231 complexes and monitored progress by native gel electrophoresis (**Figure 4G**). The top band,
232 representing the fully assembled exocytic SNARE complex, is present in both conditions but

233 disappears when adding Mg^{2+} to initiate hydrolysis and the disassembly reaction. There was no
234 qualitative difference in the disassembly between uncrosslinked and crosslinked conditions after
235 normalizing for labeling efficiency (**Figure 4H**). Thus, the folded state of the Habc domain does
236 not change during yeast SNARE disassembly, and crosslinking the Habc domain does not affect
237 the disassembly kinetics. Taken together, these results for both the yeast and neuronal systems
238 further argue against a threading model of Sso1 engagement since the Habc domain would be
239 unable to pass through the D1 and D2 domains.
240

241 **Substrate-released Sec18 structures reveal coordinated ring opening**

242 Together, these observations beg the question of how Sso1 enters the Sec18 ATPase
243 rings. To address this topological challenge, we next determined structures of the y20S complex
244 after initiating Sec18 hydrolysis by adding Mg^{2+} (referred to as "hydrolyzing condition").
245 Informed by a fluorescent protein disassembly assay (**Extended Data Figure 5H)**, we initiated
246 the disassembly reaction and waited 7 seconds before sample vitrification.
247 In the resulting cryo-EM dataset, we found a small number of particles (6,356 or 2.26%
248 of final particles, class 1) that consist of entire y20S assemblies (**Figure 5A**), largely similar to
249 those observed in the non-hydrolyzing condition (**Figure 2)**. While the resolution of this
250 reconstruction is low (10.88 Å), the D1 ring is flattened relative to reconstructions from the non-
251 hydrolyzing condition (**Figure 5B**). Considering that our sample consists of purified y20S
252 complexes before initiating disassembly by adding Mg^{2+}, this D1 ring flattening likely occurs
253 due to Mg^{2+} binding or ATP-hydrolysis at one or more subunits.
254 The remaining particles (274,883 or 97.74 % of final particles) were substrate-free
255 (classes 2–4 in **Figure 5C–E**). The D1 ring is also flat in all these substrate-free classes, with all
256 D1 protomers bound to ADP. This uniform binding to ADP, as opposed to the spiral staircase of
257 apo, ADP, and ATP-bound protomers, likely explains the flattened nature of the protomers. In
258 the D2 ring all protomers are still ATP bound, consistent with its role in oligomerization. Class 4
259 consists of a configuration where both the D1 and D2 rings are heptameric (**Figure 5C**), and
260 class 3 is similar to this heptameric class, except the 7th protomers is only partially occupied
261 (**Figure 5D).**
262 Class 2 has a well-resolved hexameric configuration with a coordinated split in class 2 in
263 the D1 and D2 rings (**Figure 5E**). This split spans ~20 Å between protomers and is large enough
264 to accommodate a polypeptide chain entering or leaving the rings. This conformational change is
265 likely induced by the nucleotide state, and specifically coupled to the presence of ADP
266 throughout the ring following hydrolysis and SNARE substrate processing; this opening allows
267 the processed SNARE substrate to be released from the side. This side-release mechanism thus
268 solves one part of the topological challenge state above; threading occurs, but the substrate exits
269 from the side, avoiding the membrane domains and linkages in SNARE proteins.
270

271 **Substrate-free Sec18 structures reveal coordinated ring opening**

272 Next, we asked if this same side-opening of Sec18 occurs in the hydrolyzing condition without
273 SNARE substrate. We prepared purified wild-type Sec18 in the presence of ATP and Mg^{2+} in a
274 three-stage procedure that yielded a pure sample used for cryo-EM studies (**Extended Data**
275 **Figure 6A-C)**. Two bands were visible in native gels, indicating two oligomeric states
276 (**Extended Data Figure 6D**). Processing and classification led to three classes, two of which
277 appeared to be heptameric and identical (280,935 particles and 73,253 particles, respectively;
278 **Figure 6A**) and the third class, which contained indeterminate density in the D1 ring (70,513
279 particles). Density for the N-domains was not well resolved in any of the classes, presumably
280 due to the conformational flexibility of the N-domains without substrate or adaptor present.

281 3D variability analysis (3DVA)[41] of the third class suggests that it consists of a mixture
282 of heptameric and hexameric Sec18 (**Extended Figure 6E),** consistent with the two bands seen
283 on a native gel of the sample**.** The hexameric class reconstructed from 3DVA particle slices from
284 the first mode (**Figure 6B**) is like class 2 observed for the y20S complex under hydrolyzing
285 conditions (**Figure 5C**), wherein hexameric Sec18 has a large, coordinated opening in its D1 and
286 D2 domain rings without substrate. This similarity in Sec18 conformations provides further
287 evidence that the substrate is both loaded and released through the side of the rings, explaining
288 why the Habc domain is not unfolded during Sec18/NSF activity (**Figure 3**) and that
289 crosslinking the Habc domain does substantially affect the disassembly kinetics (**Figure 4H**).
290 This solves the second part of the topological question stated above.
291 The heptameric class (**Figure 6A**) is nearly identical to class 4 observed in the y20S
292 complex in a hydrolyzing condition (**Figure 4A**). Each protomer in the heptamer is similar to the
293 others, with an average RMSD of <1Å between them, with the angle between the D1 and D2
294 rings varying only with a small range of 61.9°–67.1°, in contrast to hexamer, with a range of
295 60.8°–92.3° (**Figure 2C, Extended Data Figure 6F**). The D1 pore diameter is 30 Å, larger than
296 substrate-bound hexamer, with a diameter of ~11 Å. The substrate-free structures (hexamer and
297 heptamer) are nearly identical (RMSD = 0.48 Å) to the substrate-released structures.
298 To test if these D1 ADP-bound, ring-flattened states of Sec18 observed by single particle
299 cryo-EM convert to a disassembly-competent state, we tested the same protein preparation used
300 for cryo-EM with a vacuolar/lysosome proteoliposome fusion assay[42,43] (**Extended Figure 6H-J,**
301 **Supplementary Discussion**); this assay confirmed that the Sec18 preparation used for cryo-EM
302 was active and processed vacuolar SNAREs. Moreover, NSF also adopts this flattened ring state
303 and a heptameric or hexameric arrangement when exchanged into a buffer containing ATP and
304 Mg^{2+} without substrate (**Extended Data Figure 7, Supplementary Discussion**), consistent with
305 our observations that Sec18 and NSF share the same functional mechanism.
306

307 **Implications for ATPase activity**

308 The observed structures of Sec18 in substrate-free, substrate-loaded, and substrate-
309 released states suggest large conformational change upon ATP hydrolysis, consistent with

310 previous observations[3,27,44]. In the substrate-free and substrate-released states, examination of the
311 D1 nucleotide binding pockets reveals critical catalytic residues far from the nucleotide (**Figure**
312 **6C**)**.** However, in the substrate-engaged state, these conserved residues are tightly bound to
313 nucleotide in a state preceding the binding of divalent cation required to drive hydrolysis.
314 Employing the same statistical workflow used to cluster the different y20S classes (**Methods**),
315 we identified the most significant residues that vary between the no substrate and substrate-
316 bound state by generating an ensemble of models for each class via ensemble refinement
317 (residues colored red in **Figure 6D,** variance contribution per component in **Extended Figure**
318 **5I**). For both the arginine finger loop and Walker B motif, we observed substantial changes to
319 side chain and backbone conformations (**Figure 6E-F**), wherein coordinating residues are
320 positioned closer to the nucleotide-binding pocket in the presence of substrate, presumably
321 establishing a hydrolysis-ready state. In the case of the arginine fingers, the side chain
322 conformational change is likely coupled to nucleotide identity, as hydrolysis disrupts phosphate
323 coordination with ATP, weakens the interprotomer interface, and leads to rigid body motion of
324 the D1 large subdomain as the arginine fingers disengage. The case of the shift in the Walker B
325 element, on the other hand, appears to be the flexing of the loop without substantial changes to
326 the sidechains of D349 and E350, induced by the motions of pore loop 2 (GVG motif) that bind
327 to the substrate in the pore.

328 **Discussion**

329 Based on our LC-MS/MS, structural, and functional results, we propose the following
330 model for SNARE recycling (**Figure 6G**), consisting of four phases. Sec18/NSF transiently
331 forms split-open conformation of both D1 and D2 rings in the resting phase with no substrate.
332 Once the *cis*-SNARE complex has been coated with adaptor Sec17/α-SNAP molecules, the
333 Sec18 N-domains can bind the subcomplex and position the unstructured linker connecting the
334 N-terminal Sso1 Habc domain to the SNARE domain proximal to the D1/D2 split, thus
335 promoting the loading of substrate into the catalytic core of the enzyme. More generally, this
336 side-loading mechanism would allow Sec18/NSF to process complexes incorporating all
337 SNAREs in the cell regardless of the presence of folded N-terminal domains, provided that, in
338 the latter case, a long enough linker connects them to the following SNARE domain. Upon the
339 formation of the 20S particle, ATP-driven hydrolysis likely fuels the disassembly of the SNARE
340 complex by some degree of threading, accompanied by D1 ring flattening. In the case of Sso1,
341 since full threading cannot occur due to the transmembrane domain, partial melting of the N-
342 terminal end of the SNARE domain could be sufficient to destabilize the SNARE complex.
343 Finally, the pore-bound SNARE is released through the side-split of the D1 and D2 rings,
344 regardless of membrane anchors or transmembrane domains in SNARE proteins. This model
345 explains how Sec18/NSF can disassemble SNAREs with constrained topologies.
346
347 As observed in our cross-linking LC-MS/MS experiments (**Figure 1**), the Sec18 D2 ring
348 can interact with not just with the Habc domain of Sso1 but also with other N-terminal accessory

349 domains (GOS1, TLG1, TLG2, etc). In turn, N-terminal domains often interact with other
350 factors. For example, the trimeric Dsl1 complex binds to the SNAREs Use1, Ufe1, and Sec20
351 through interactions with N-terminal SNARE domains. This 255 kDa complex tethers
352 endoplasmic reticulum membranes together before forming the *trans*-SNARE complex and
353 likely remains complexed before, during, and after fusion[32]. Another example is HOPS, a
354 hexameric complex that tethers lysosomal/vacuolar membranes and orchestrates their fusion[45].
355 HOPS has two Rab-binding subunits for tethering and a SNARE binding subunit that catalyzes
356 initial SNARE complex assembly[46]. Sec18/NSF and Sec17/α-SNAP cooperate with HOPS to
357 ensure rapid and efficient SNARE-mediated fusion[47,48]. For the case of Dsl1, the N-terminal
358 domains of SNAREs remain in a supramolecular arrangement that must be bypassed. For
359 vacuolar/lysosomal fusion, SNAREs must be preprocessed and handed off to the HOPS
360 complex. These complexes pose topological constraints on both ends of the SNAREs that can be
361 resolved by side-loading and side-release.
362
363 Finally, we note that distantly related AAA+ clamp loaders and their clamp load their
364 nucleic acid substrate from the side as well[49]. DNA is loaded into a split opened clamp and
365 AAA+ clamp loader. Once the clamp loader recognizes the substrate, the ATPase is triggered,
366 and the clamp loader closes the complex around the DNA. Once the clamp is fully secured, the
367 clamp-loader is then released. This shared mechanism suggests the possibility of side-loading
368 and release across the entire AAA+ protein family.
369
370 In summary, Sec18/NSF can load and release SNARE substrates via a coordinated
371 opening in the D1 and D2 rings. This mechanism does not preclude the more conventional notion
372 of complete substrate threading through the pores of Sec18/NSF if the SNARE substrate is not
373 topologically restricted by membrane domains or anchors or by N-terminal domains or
374 complexes. However, considering these topological considerations are ubiquitous for SNAREs,
375 the side-loading/release mechanism is likely conserved for the entire Sec18/NSF class of AAA+
376 proteins.
377

378 **Figure Legends**

379 **Figure 1: *In vivo* crosslinking mass-spectrometry of Sec18**
380 **a,** Top left: Venn diagram of proteins found in the condition without crosslinking agent (red)
381 added and with crosslinking agent added (green). Bottom right: SAFE-analysis[34] of yeast
382 proteins that specifically crosslink to Sec18. Blobs represent enrichments in the pathway. Blobs
383 of different colors represent enrichments that are specific to different p-value thresholds (brown
384 < 0.01, blue < 0.001, red < 0.0001). **b,** Heatmap of yeast SNARE proteins crosslinking to
385 specific Sec18 positions. The Sec18 primary sequence along the x-axis is colored coded by
386 domain, and yeast SNARE proteins with at least one medium confidence crosslink are shown
387 along the y-axis. Red squares represent positions where one or more manually verified, high-

confidence crosslinks were found (**Methods**). Orange squares represent where one or more manually verified medium-confidence crosslinks were found. White squares represent positions in which manually verified crosslinks were not found or were of low confidence. **c-f,** Crosslinking schematic of Sec18 and SNAREs that contain at least one high-confidence crosslink to the Sec18 D2 domain. Red dashed lines represent high-confidence crosslinks, and orange dashed lines represent medium-confidence crosslinks.

Figure 2: The y20S supramolecular complex

a, Domain diagrams of the components used to prepare the y20S complex; coloring follows this throughout (top left). The structure of class 1 of y20S, with ATP and ADP nucleotides (red and blue, respectively; bottom right). Cryo-EM density for class 1 and the Sso1 atomic model around residue F173 (inset, bottom left). **b,** Sso1 substrate is engaged by Y315 in all D1 protomers with bound nucleotide. **c,** Conformations of the protomers of Sec18 when engaged to substrate. D, Top-down views of class 1 and class 8 cryo-EM maps. **e,** Cartoon top-down views of eight y20S classes, which differ primarily by spire configuration, *i.e.*, the pattern of N-domain and α-SNAP engagement.

Figure 3: Sso1 is threaded through the D1 and D2 domains

a, y20S class 1 atomic model emphasizing the position of Sso1. Stars represent the crosslink identified by crosslinking mass spectrometry (**Figure 1B**). **b,** Bottom view of y20S class 1 D1 ring; the Habc domain is packed against the D2 ring surface, between protrusions corresponding to the C-terminal helical regions of two D2 small subdomains. All surfaces are colored grey, except for protomers A and B, which are colored by their electrostatic potential **c,** Rotated view of y20S class 1 relative to **b** showing the Habc tucked between protomers A and B with now the Habc domain colored by its electrostatic potential **d,** Composite cryoEM map (blue, Relion-unsharpened map: Habc domain and D1 density and CryoSPARC 3DFlex map: D2 density) of y20S class 1. Nucleotides are shown as red (ATP) or blue (ADP) spheres. **e,** Cryo-EM maps of all eight y20S classes reveal the Habc domain associated with the Sec18 D2 ring in all classes (red). In 6/8 classes, the Habc density is radially averaged into multiple discrete positions around the D2 ring, leading to more diffuse density.

Figure 4: Sec18/NSF does not unfold the Habc domain

a, Diagram of the smFRET disassembly/re-assembly assay with linked neuronal SNAREs. The linked SNAREs are either stochastically labeled within the SNARE domains or the syntaxin Habc domain. **b,** Representative traces of labeled neuronal SNARE complex in the non-hydrolyzing condition. Violet represents the acceptor, and orange represents the donor-dye fluorescence-intensity time traces. n = 53. **c,** Representative time trace of labeled SNARE complex in disassembly conditions, the black line represents fitting by a vbGMM[50]. n = 114. **d,** Representative time-trace of labeled Habc domain in the non-hydrolyzing condition. Green represents the donor, and red is the acceptor dye fluorescence intensity time-traces. n = 27. **e,**

428 Representative time-trace of labeled Habc domain in disassembly conditions. The black line
429 represents fitting a vbGMM. n = 22. **f,** Histograms of E-FRET for all four conditions. The blue
430 dotted line represents a Gaussian fit of the data. The y-axis is the normalized frequency of
431 occurrence of the E-FRET states in the traces. Top left: SNARE E-FRET for the non-
432 hydrolyzing condition, top right: SNARE E-FRET for the hydrolyzing condition. Habc E-FRET
433 for the non-hydrolyzing condition (bottom left). Habc E-FRET for the hydrolyzing condition
434 (bottom right). **g,** Native gel of labeled uncrosslinked or crosslinked yeast SNARE complex that
435 has been labeled with Oregon Green Maleimide 488. **h,** Quantification of gel densitometry of n =
436 3 independent disassembly experiments. Error bars represent the standard deviation of the mean.
437 Densitometries were all normalized to 0 min values.
438
439 **Figure 5: Post-disassembly of y20S reveals substrate-released states**
440 **a,** Cryo-EM map of y20S in the hydrolyzing condition, colored by domain. **b**, The distance
441 between the D1 and D2 domains decreases for some protomers under hydrolyzing conditions,
442 leading to D1 ring flattening. The orange model corresponds to protomer E from the merged
443 D1/D2 focused class in the non-hydrolyzing condition, which was rigid-body fit into the density
444 of the hydrolyzing condition to generate the blue model. **c,** Cryo-EM map and model of class 4
445 of Sec18, showing a heptamer. **d,** Cryo-EM map and atomic model of class 3 of Sec18,
446 suggesting a transition state. **e, Cryo-**EM map and atomic model of class 2 of Sec18, showing a
447 split hexamer. In panels **c-e**, the top is the EM-map, while the middle and bottom show atomic
448 models in top and side views, respectively.
449
450 **Figure 6: Structures of substrate-free Sec18 in the hydrolyzing condition**
451 **a,** Atomic model of the substrate-free heptameric state of Sec18 (class 1). **b,** Atomic model of
452 the split substrate-free hexameric state of Sec18 (derived from 3DVA of class 3). **c,** The D1
453 nucleotide binding pocket is remodeled as a function of SNARE substrate binding and nucleotide
454 state. The arginine fingers R406 and R409 are contributed by the neighboring protomer. The
455 substrate-free and substrate-released states are nearly identical in conformation. Water molecules
456 are shown as red spheres. **d**, Atomic model of Sec18 with protomer A colored blue if not a
457 significant residue from conformational analysis and colored red if significant (p-value < 0.05).
458 **e,** Atomic models showing the difference of the arginine finger loop in the no substrate
459 (transparent) and substrate condition. **f,** Atomic models of the loop proximal to the Walker B
460 motif in the no substrate (transparent) and substrate condition. For **d-f**, residues are colored red if
461 they are in the top 5% of residues that significantly vary between conditions. **g.** We propose a
462 general model of SNARE recycling, regardless of the cellular context. First, a *cis*-SNARE
463 complex is coated with at least 1 Sec17/α-SNAP adaptor molecule, allowing Sec18/NSF to
464 recognize it. The SNARE substrate is then loaded into a split hexamer with a coordinated
465 opening in both D1 and D2 rings through the side, bypassing whatever N-terminal domains may
466 be present. The substrate is then threaded coaxially through the Sec18/NSF pore. Upon
467 completion of processing, the SNARE substrate is released through the side, bypassing the

468 topological constraints of the membrane. Finally, Sec18 returns to its 'resting' state until more
469 substrate is encountered. Yellow arrows indicate the direction of loading and release.
470
471

472 **Extended Data Figure Legends**

473

474 **Extended Data Figure 1: In vivo mass-spec workflow and additional analysis**
475 **a,** Workflow of how samples were processed before mass-spec. **b,** Representative mass-
476 spectrometry raw data of high confidence **(Methods)**, suggesting that the Habc domain is
477 crosslinked to the D2 domain. In the sequence diagram, the cross-linked lysine residues are
478 shown in orange.
479

480 **Extended Data Figure 2: Purification and assembly of y20S complex**
481 **a,** Sec18 SDS-PAGE gel after the final SEC run. Pooled fractions were frozen and stored. **b,**
482 Sec17 SDS-PAGE gel after final SEC run. Pooled fractions were frozen and stored. **c,** Schematic
483 of y20S assembly. Snc1, Sso1, and Sec9 were purified individually before being co-folded for
484 complex formation (**Methods**). The resulting SNARE complex was added to purified Sec17,
485 EDTA was added, and then purified Sec18 was added. The resulting y20S complex was purified
486 by SEC, and fractions were pooled. The final gel shows reference inputs for Sec18, Sec17, and
487 yeast SNARE complex, the final concentrated y20S complex, and the fractions from SEC that
488 were pooled (yellow lines).
489

490 **Extended Data Figure 3: Intra and inter-protomer crosslinks mapped on the y20S complex**
491 **structure**
492 **a,** Two Sec18 protomers of the y20S complex are shown. The black dashed lines represent
493 crosslinks designated as excellent (passing all manual verifications) and superimposed over the
494 diagram. The two insets show inter-protomer crosslinks. **b,** Electrostatic surface potentials of the
495 interaction between SNAREs and Sec17. Negatively charged regions are colored red, and
496 positive ones are colored blue. **c,** Electrostatic surface potentials of the interaction between
497 Sec17 and the N-domains of Sec18. Alternating views of these interactions are shown to
498 demonstrate the complementarity of the electrostatic interactions.
499

500 **Extended Data Figure 4: Sequence and structural conservation between NSF and Sec18**
501 **a,** Primary sequence alignment between NSF *c. griseus* and Sec18 *s. cerevisiae.* **b,** cartoon
502 representation of an atomic model of Sec18 D1/D2 focused model colored by Cα root-mean-
503 square-difference (RMSD) to the structure of the binary SNARE complex with NSF and α-
504 SNAP[27]. **c,** Focused view of substrate in D1**.** The substrate bound to the D1 pore is represented
505 as spheres.
506

507 **Extended Data Figure 5: Cross-complementation disassembly assays**
508 **a,** Scheme of fluorescent-protein labeling. Snc1 was labeled with mTurq, and SSO1 was labeled
509 with mVenus (**Methods**, referred to as fpySNARE). **b**, SDS Page gel of the final SEC
510 purification of y20S complex. **c,** Representative traces from the disassembly assay (**Methods**).
511 The mTurq emission is monitored, and an increase in emission as the complex suggests that
512 SNARE disassembly occurs (loss of fluorescence resonance energy transfer to mVenus upon
513 disassembly). **d-e**, Disassembly plots of SNAREs and NSF/Sec18 combinations. **f,** Residues that
514 were replaced with p-azido-l-phenylalanine are shown as yellow spheres in a black box **g,** MS
515 raw data of double crosslinked yeast exocytic SNARE complex. **h,** Michaelis-Menten diagram of
516 the y20S disassembly reaction. The red line shows the fitted line used to calculate M-M metrics,
517 whereas the black points and error bars show the actual data. i, Variance contributed by each
518 principal component.
519
520 **Extended Data Figure 6: Functional studies of Sec18.**
521 **a,** Schematic of purification of Sec18. **b,** SDS-PAGE gel of final SEC fractions and the fractions
522 that were pooled for CryoEM studies of the y20S complex and the vacuolar fusion assay. **c,**
523 Corresponding SEC trace showing the Sec18 oligomer eluting at expected volume. **d,** Native gel
524 of final sample showing two oligomeric species. **e,** Representative slices of class 3 of the y20S
525 complex under the hydrolyzing condition, subjected to 3DVA revealing split hexamer class. **f,**
526 Alignment of all seven protomers, where each protomer is colored uniquely. **g,** Cartoon depicting
527 the large pore in the heptameric state of the y20S complex under the hydrolyzing condition. **h,**
528 Cartoon of the vacuolar fusion assay [42,43] (**Methods**) used to determine the function of the same
529 Sec18 sample used for CryoEM studies of the y20S complex. Fusion only occurs when Sec18
530 prepares SNAREs for fusion, leading to fluorescence. **i,** Representative traces of fusion activity.
531 **j,** Dot-plots of all activity assays.
532
533 **Extended Data Figure 7: CryoEM structures of substrate-free NSF in the hydrolyzing**
534 **condition**
535 **a-d,** CryoEM maps (sharpened cryoSPARC) in three orientations (top to bottom rows) of the
536 four classes of NSF in the hydrolyzing condition. The NSF heptamer (class 1) is designated as
537 class 1. Classes 2-4 showed hexameric NSF in similar orientations with varying resolution for
538 the substrate, so the best one, class 3 (initial) (c), was chosen for 3DVA analysis in CryoSPARC.
539 **e,** The main principal component of the 3DVA analysis was used to select a subset of particles
540 clearly showing an NSF N-terminal domain that is engaged with the D2 ring and then re-refined
541 against this subset of particles to yield the final map for class 3. **f-g,** insets showing that an N-
542 domain acts as a bound substrate in class 3 (final).
543

544 **Methods**

545 **HA-Sec18 *S. cerevisiae* strain preparation and treatment**

546 Briefly, we created an *S. cerevisiae* strain containing HA-tagged Sec18 and treated it with
547 zymolyase and lyticase to dissolve its cell wall but maintain its integrity as a living cell
548 (spheroplast). We then incubated the spheroplasts with disuccinimidyl glutarate (DSG), a
549 membrane permeable protein crosslinking agent, for 30 minutes before cellular lysis and anti-HA
550 co-immunoprecipitation (coIP) to isolate Sec18 and any bound proteins to it. This sample was
551 then subjected to SDS-PAGE gel electrophoresis, and the bands corresponding to crosslinked
552 Sec18 were excised and sent for liquid chromatography-mass spectrometry (LC-MS/MS)
553 analysis. More specifically, tagged Sec18 (pYK175, 3x-Flag N-terminal, HA-tag C-terminal)
554 plasmid was transformed into *S. cerevisiae* S288C using the Frozen-EZ Yeast Transformation
555 Kit (Zymo Research T2001). Expression of tagged Sec18 was accomplished by growing yeast in
556 1% raffinose and 1% galactose media. Cells were spun down and treated with 100 units of
557 zymolyase (Zymo Research #1004) at 37°C for 1 hour. After incubation, spheroplasts were
558 pelleted with a 1000 xg spin. DSG diluted in 1x PBS was used to resuspend the pellet, and the
559 sample was incubated for 30 minutes. The excess DSG was then quenched with 1M Tris and
560 incubated for another 15 minutes. Cells were washed with cold PBS and were resuspended in
561 lysis buffer (5mM EDTA, 1mM ATP, 1mM TCEP, 150 mM NaCl, 10% glycerol, 0.5% NP40,
562 and 50 mM HEPES pH 7.4) and glass beads (BioSpec 11079105). This bead-lysis-cell solution
563 was vortexed for 5 minutes at 4°C three times with ice incubations between each vortexing. The
564 solution was then spun down at 10,000 xg for 5 minutes at 4°C. The supernatant was taken and
565 then spun down again at 10,000 xg for 15 minutes at 4°C. The supernatant was then taken and
566 subjected to magnetic-bead anti-HA coIP (Thermo Scientific 88838). The eluant of the beads
567 was run on an SDS-PAGE gel, and the bands corresponding to Sec18 were excised.
568
569
570 **XL-MS sample preparation**
571 Protein samples were embedded in Coomassie-stained gel bands, fixed in 1% acetic acid.
572 The gels were washed several times in 50 mM ammonium bicarbonate, followed by reduction
573 with 10 mM of dithriothreitol (DTT) and incubation for twenty minutes at room temperature.
574 They were then alkylated using 30 mM acrylamide for 30 minutes. This was proceeded by
575 overnight digestion at 37 degrees Celsius with 500ng of mass spectrometry grade trypsin/LysC
576 mix (Promega). Post-digestion, samples were quenched with formic acid (adjusted to a pH ~3)
577 and desalted using MonoSpin C18 Solid-Phase Extraction (SPE) columns (GL Sciences).
578 Finally, the samples were dried via SpeedVac (Thermo Scientific, San Jose, CA) and exchanged
579 into LC-MS reconstitution buffer (2% acetonitrile with 0.1% formic acid in water) for
580 instrumental analysis.
581
582
583 **LC-MS/MS analysis**
584 Mass spectrometry experiments were performed using an Orbitrap Eclipse Tribrid mass
585 spectrometer (Thermo Scientific, San Jose, CA) attached to an Acquity M-Class UPLC system

586 (Waters Corporation, Milford, MA). The UPLC system was set to a flow rate of 300 nL/min,
587 where mobile phase A was 0.2% formic acid in water and mobile phase B was 0.2% formic acid
588 in acetonitrile. The analytical column was prepared in-house with an I.D. of 100 microns pulled
589 to a nanospray emitter using a P2000 laser puller (Sutter Instrument, Novato, CA). The column
590 was packed with Dr. Maisch 1.9 micron C18 stationary phase to a length of approximately 25
591 cm. Peptides were directly injected into the column with a gradient of 3-45% mobile phase B,
592 followed by a high-B wash over a total of 80 minutes. The mass spectrometer was operated in a
593 data-dependent mode using CID fragmentation for MS/MS spectra generation.
594 The RAW data were analyzed using Byonic v5.2.5 (Protein Metrics, Cupertino, CA) to
595 identify peptides and infer proteins. Initial Byonic analyses used a concatenated FASTA file
596 containing the Uniprot *Saccharomyces cerevisiae* proteins and other likely contaminants and
597 impurities. Once sample complexity was determined, a second round of Byonic analyses was
598 completed using a targeted FASTA file, which included only the sequences present in the samples
599 and allowances for crosslinked peptides with the appropriate linker. Proteolysis with Trypsin/LysC
600 was assumed to be fully specific with up to two missed cleavage sites. The precursor ion tolerance
601 was set to 12 ppm. The fragment ion tolerance was set to 0.4 Da. Cysteine modified with
602 propionamide was set as a fixed modification in the search. Variable modifications included
603 oxidation on methionine and acetylation on protein N-terminus. Proteins were held to a false
604 discovery rate of 1% using the standard reverse-decoy technique (Elias & Gygi Nat. Meth. 2007).
605 Potential crosslinked peptides were then validated and graded as described previously
606 using Byologic v5.2.31 (Protein Metrics) (Kobilka & Benovic, Cell, 2017). Briefly, a series of
607 empirical constraints were used for inspection, including minimum peptide and crosslink partner
608 length, chromatographic profile, MS1 coelution and MS/MS spectrum fragmentation quality.
609 Following this, identified crosslinked peptides were further categorized into three groups: high
610 confidence, medium confidence, and low confidence, where "high confidence" succeeded on all
611 these rules and "low confidence" failed at least in three of these rules.
612
613
614 **Preparation of y20S in the non-hydrolyzing condition**
615 The y20S complex consists of the Sso1–Snc1–Sec9 SNARE (ySNARE) complex, the
616 Sec18 oligomeric complex, and Sec17 adaptor proteins, and it was assembled in a multi-stage
617 workflow. Starting with the yeast exocytic complex, individual SNARE components Sec9 (401-
618 651), Sso1 (1-265), and Snc1 (1-93) were purified individually. All three proteins were cloned
619 into the pET28b plasmid vector with a 6x-His tag and a TEV cleavage sequence N-terminal to
620 the SNARE protein sequence.
621 For Sec9, we used a lysis buffer of pH 7.5, 50 mM NaPi, 300 mM NaCl, 10 mM
622 Imidazole, 0.5 mM TCEP, 1% Triton X-100 and SIGMAFAST Protease Inhibitor Cocktail
623 Tablet (Sigma-Aldrich S8830) which was used to resuspend bacterial cell pellets from an 8L
624 culture of auto-induced One Shot BL21 (DE3) *E*. coli (Thermofisher C600003). This
625 resuspended lysate was subjected to sonication for 20 minutes (3 seconds on, 9 seconds off, 60%

626 amplitude), followed by a 30-minute 4000 xg spin and a 1-hour 40,000 xg spin. The supernatant
627 was bound (1 hour, 4°C), run through a Ni-NTA column, and washed with pH 7.5, 50 mM NaPi,
628 30 mM Imidazole, 300 mM NaCl, and 0.5 mM TCEP buffer. The sample is then eluted with a
629 pH 8 50 mM NaPi, 400 mM Imidazole, 300 mM NaCl, and 0.5 mM TCEP buffer. This sample is
630 then digested overnight with TEV protease in a dialysis buffer (pH 8 20 mM Tris, 250 mM
631 NaCl, 0.5 mM TCEP, and 1 mM EDTA). The cleaved sample was then subjected to a MonoS
632 5/50 GL with buffer A consisting of pH 8 20 mM Tris, 50 mM NaCl, 0.5 mM TCEP, 1mM
633 EDTA and with buffer B consisting of pH 8 20 mM Tris, 500 mM NaCl, 0.5 mM TCEP, and
634 1mM EDTA. Taking the majority peak corresponding to Sec9, we then subjected this peak to
635 size exclusion chromatography (SEC) with the HiLoad 16/60 Superdex 200. The peak
636 corresponding to Sec9 was concentrated and flash-frozen. We followed the same protocol for
637 individually purifying Snc1 and Sso1.
638 Once all three individual SNAREs were purified, a 1:1:1 molar ratio of these proteins
639 was added to a 6M GdHCl solution. This solution was then slowly dialyzed overnight at 4°C into
640 a solution of 250 mM NaCl, 50 mM HEPES pH 7.6. This sample was then diluted to a NaCl
641 concentration of 75 mM and then subjected to MonoQ with the low salt buffer at 75 mM and the
642 high salt buffer at 500 mM with both buffers in 50 mM HEPES pH 7.6. The peak corresponding
643 to a 1:1:1 ratio of all three bands, indicative of the yeast exocytic complex, was then
644 concentrated for y20S formation without freezing.
645 The complete Sec18 protein coding sequence was cloned into the pMZ0002/pYK103
646 backbone with a 6x-His tag and TEV cleavage sequence N-terminal to Sec18. The 8L culture of
647 One Shot BL21 (DE3) *E.* coli (Thermofisher C600003) was spun down and resuspended in lysis
648 buffer of pH 7.5 100 mM HEPES, 500 mM KCl, 5 mM ATP, 5mM $MgCl_2$, protease inhibitor
649 tablets, and benzonase. This lysate was sonicated for 20 minutes (3 seconds on, 9 seconds off,
650 60% amplitude) and clarified with a 45,000 xg spin for 30 minutes. The lysate was supplemented
651 with 20 mM Imidazole bound to Ni-NTA beads (4°C) and washed with pH 7.5 20 mM HEPES,
652 480 mM KCl, 0.5 mM ATP, 0.5 mM TCEP, 20 mM Imidazole, 1 mM $MgCl_2$, and 10% glycerol.
653 The sample was then eluted with pH 7.5 20 mM HEPES, 480 KCl, 0.5 mM ATP, 0.5 mM TCEP,
654 500 mM Imidazole, 1 mM $MgCl_2$, and 10% glycerol. The protein-containing peak was then
655 equilibrated in SEC buffer pH 6.8 20 mM PIPES, 125 mM KCl, 0.2M sorbitol, 5 mM $MgCl_2$, 2
656 mM ATP, 2 mM DTT, and 10% glycerol and injected a HiLoad 16/60 Superdex 200. The
657 fractions were pooled, concentrated, and snap-frozen for later usage. The band right below Sec18
658 is an oligomeric *E. coli* contaminant, which is removed in the final steps of y20S complex
659 purification (**Figure S2A, C**). Moreover, this contaminant is absent in the protocol for preparing
660 high-purity Sec18 (see below and **Figure S6B**).
661 The full Sec17 coding sequence was cloned with a 10x-His tag and a TEV cleavage
662 sequence fused N-terminally. The 8L culture of One Shot BL21 (DE3) *E. coli* was spun down
663 and resuspended in a lysis buffer of pH 8 50 mM NaPi, 300 mM NaCl, 20 mM Imidazole, and
664 0.5 mM TCEP. This mixture was then sonicated (3 seconds on, 9 seconds off, 60% amplitude)
665 and clarified at 45,000 xg for 30 minutes. This supernatant was then incubated with Ni-NTA

666 beads for an hour and then washed with lysis buffer. The protein was eluted with lysis buffer
667 supplemented with 500 mM Imidazole and 5 mM EDTA. TEV protease was added to pooled
668 fractions and slowly dialyzed overnight at 4°C against a pH 8 50 mM Tris, 100 mM NaCl, 1 mM
669 EDTA, 0.5 mM TCEP buffer. This sample was then diluted to a NaCl concentration of 50 mM
670 and run on a MonoQ 10/100 from a 50 mM to 500 mM salt gradient. The major peak
671 corresponding to Sec17 was then pooled and injected into a HiLoad 16/60 Superdex 200 SEC.
672 The major peak from this run was taken, pooled, and snap-frozen for later usage.
673 To assemble the entire y20S complex, Sec17 was added to the freshly prepared yeast
674 exocytic SNARE complex, followed by EDTA quenched Sec18 with a final ratio of
675 Sec18:SNARE:Sec17 at 1:1.67:10, where a total of 5580 picomoles of Sec18 was used, in the
676 following buffer: pH 8 50mM Tris, 150 mM NaCl, 1 mM TCEP, 1 mM ATP, and 1 mM EDTA.
677 Following this assembly, this mixture was injected onto a Superose 6 10/300 increase column,
678 and the peak corresponding to the y20S complex, as assessed by elution volume and
679 corresponding SDS-PAGE gel, was concentrated to ~40 mg/mL.
680
681 **Single particle Cryo-EM grid preparation of y20S in the non-hydrolyzing condition**
682 Quantifoil R1.2/1.3 200 mesh gold grids were treated with chloroform and dried
683 overnight. Grids were glow discharged, and 5 microliters of the sample (at a final concentration
684 of 20 mg/mL with 0.05% v/v Nonidet P-40) was blotted onto the grids and further blotted and
685 vitrified in liquid ethane using an FEI Vitrobot (ThermoFisher Scientific). Grids were blotted for
686 4 seconds with a 5-second wait time (reduced to 3 seconds in hydrolyzing condition).
687
688 **Sample preparation and single particle Cryo-EM of y20S in the hydrolyzing condition**
689 Samples were prepared identically to y20S in the non-hydrolyzing condition, except that excess
690 $MgCl_2$ was blotted onto grids immediately before vitrification, and the total blot and wait time
691 was reduced to 7 seconds before freezing.
692
693 **Sample preparation and single particle Cryo-EM of substrate-free Sec18 in the hydrolyzing**
694 **condition**
695 To prepare high-purity, substrate-free Sec18, an alternative protocol was required since
696 low-purity Sec18, which can form y20S, was not amenable to high-quality cryo-EM studies. We
697 used a protocol similar NSF[18], but at the final reassembly step, we used $MgCl_2$ instead of EDTA.
698 The cryo-EM studies were performed similarly to the studies of Y20S in the non-hydrolyzing
699 condition.
700
701 **Sample preparation and single particle Cryo-EM of NSF in the hydrolyzing condition**
702 A sample of high-purity NSF was prepared, as described in the previous section. This
703 sample was exchanged into a buffer supplemented with 1mM magnesium chloride instead of
704 EDTA and incubated before a final SEC and freezing.
705

706 **Single particle cryo-EM data collection, processing, and model building**
707 Single particle cryo-EM data collection and processing workflow are described
708 thoroughly in the **Extended Table 1** and **Supplementary Figure 2**. An FEI Titan Krios
709 (ThermoFisher Scientific) cryo-electron microscope with either a K3 Gatan or a Falcon F4i
710 camera was used for data collection. Micrographs were analyzed using a combination of initial
711 Relion 3.1[51] processing followed by additional rounds of 3D classification or heterogenous
712 refinement, and final refinements in CryoSPARC v4[52]. A general workflow description is
713 provided in **Supplementary Figure 2,** and specific dataset information is provided in
714 **Supplementary Figures 2-6** as well.
715 y20S models were constructed by first docking the crystal structure of the exocytic
716 SNARE complex (PDB ID: 3B5N) and AlphaFold2[53] models for Sec17 into the unsharpened
717 density first obtained in Relion 3.1[51]. Next, sharpened cryoSPARC-v4[52] maps were then used to
718 model the Sec18 complex and the region of Sso1 that extended from the spire into the D1 pore.
719 For class 1, 3DFlex analysis in cryoSPARC-v4 was performed. A mixture of the Relion 3.1 and
720 cryoSPARC-v4 unsharpened and sharpened maps, and the 3Dflex map were used to model the
721 Habc domain outside of the D2 ring. The resulting atomic models were iteratively refined with a
722 combination of COOT[54], Phenix real-space refinement[55], and ISOLDE[56].
723 Models of substrate-free Sec18 and NSF were built *de novo* in COOT using cryoSPARC
724 sharpened maps, and iteratively refined with ISOLDE and Phenix.
725
726 **smFRET disassembly/re-assembly assay**
727 smFRET assays with linked neuronal SNAREs, NSF, α-SNAP, and reagents were
728 prepared as previously reported[14]. Briefly, linked SNARE complex (L-SNARE) composed of
729 SNAP25A, synaptobrevin-2, and syntaxin-1A were biotinylated and flowed onto the chamber
730 that was passivated by 10 mg/mL egg phosphatidylcholine 50 nm liposomes coated with 1
731 mg/mL of biotinylated BSA to mimic the lipid environment inside the cell. 0.1 mg/mL
732 streptavidin was added to surface-tether the biotinylated and labeled L-SNARE complexes. L-
733 20S was then assembled by first adding αSNAP and then later NSF (if in disassembly
734 conditions). L-SNARE was diluted such that about 500 molecules of L-SNARE per 45 x 90 μm^2
735 field of view was visible. The raw data was imported into tMaven[44] for analysis. The standard,
736 recommended tMaven workflow was employed. Traces were not subject to any preprocessing
737 workflow. Automatic photobleach detection was used to determine the locations of
738 photobleaching, and a vbGMM mixture model was used to detect the different states.
739
740 **Crosslinking assays**
741 Cysteines were introduced into Sec9 and Sso1 for labeling with Oregon Green Maleimide
742 488 (O6034). UAG stop codons were introduced at V57 and F83 in Sso1 for crosslinking. Cys-
743 Sec9, Cys-Sso1 (with or without stop codon depending on if used for crosslinked), and 6x-His-
744 TEV-Snc1 were co-expressed (if crosslinked, also transformed with pEVOL-pAzF AddGene
745 #31186, 2mM AzF and 0.2% v/v arabinose) and induced with IPTG. Cell pellets were lysed with

746 pH 7 50 mM Tris, 200 mM NaCl, 1% v/v Triton X-100, 20 mM Imidazole, 0.5 mM TCEP and
747 protease inhibitor tablets. Lysate was sonicated for 20 minutes (3 seconds on, 9 seconds off, 60%
748 amplitude) and then clarified at 40,000 xg for 30 minutes. Following a 1-hour incubation at 4°C,
749 the beads were washed with two different buffers. Buffer 1 is simply a lysis buffer without
750 Triton X-100, and Buffer 2 is a high salt wash of pH 7 50 mM Tris, 1M NaCl, 50 mM Imidazole,
751 0.5 mM TCEP. The complex was eluted with pH 7 50 mM Tris, 200 mM NaCl, 350 mM
752 Imidazole, and 0.5 mM TCEP. The sample was then digested overnight with TEV protease and
753 dialyzed into pH 7 20 mM Tris, 200 mM NaCl, 0.5 mM TCEP. This sample was then injected
754 onto a HiLoad 16/60 Superdex 200. The fractions containing all three in equimolar ratios were
755 taken and concentrated. Samples were labeled with Oregon Green Maleimide 488 in molar
756 excess overnight before cleanup with a Zeba spin column (ThermoFisher 89889). If the sample
757 was meant to be crosslinked, it was subjected to UV irradiation before Oregon Green Maleimide
758 labeling.
759 For native gel disassembly assays, reactions were assembled in test tubes, initiated with
760 $MgCl_2$, and quenched with EDTA. Samples were then loaded into Any kD Mini-Protean gels
761 (Bio-Rad 4569033) and used Tris-glycine running buffer (Bio-Rad) supplemented with 1 mM
762 ATP to prevent Sec18 from falling apart in the gel. Gels were first visualized in an iBright 1500
763 (ThermoFisher Scientific) to visualize ySNARE bands only before coomassie staining. Gel
764 densitometry was assessed in ImageJ.
765
766 **FRET and fluorescent dequenching disassembly assays**
767 Neuronal disassembly assays were carried out as previously reported[10,45], leveraging
768 fluorescence dequenching of the neuronal SNARE complex labeled with Oregon Green
769 Maleimide 488. For yeast SNARE disassembly assays, a strategy was devised to tag Snc1 with
770 mTurq and Sso1 with mVenus. When assembled, excitation by a 434 nm laser leads to mVenus
771 emission. 434 nm laser excitation leads to mTurq emission. Disassembly is followed by
772 monitoring excitation/emission at 434/474 nm such that as the SNARE complex is disassembled,
773 mTurq emission increases. We used the same instrument (FlexStation II 384, Molecular Devices)
774 and a 384-well format to perform both the dequenching and FRET assays that were initiated by
775 titrating $MgCl_2$ in excess of the reactions.
776
777 **Structural analysis**
778 Statistical structural analysis was performed to identify the most significant backbone
779 motions between the many different structural states observed. Using Python 3, principle
780 component analysis (PCA) on backbone ϕ/ψ angles was performed, and the single mode that
781 contributed most to the variance (>70%) was analyzed. y20S models were then clustered in this
782 reduced 5-dimensional space. When comparing the substrate-free and substrate-engaged states,
783 ensembles consistent with a given map were generated to avoid model-building bias using
784 Phenix's simple molecular dynamics implementation for 2000 steps followed by a round of
785 phenix.refine[55]. These ensembles were then subjected to backbone ϕ/ψ PCA, and the mode that

contributed to the largest variance between the two clusters for the two classes was used to determine which residues contributed most to the difference in structures.

Vacuolar fusion assay

Assays were performed as previously reported[42,43] with the same substrate-free Sec18 protein sample/batch that was purified and used for CryoEM. Briefly, proteoliposomes with vacuolar SNAREs were prepared with either Phycoerythirin-biotin (PhycoE) or Cy5 and incubated in a fluorescence plate reader for 40 minutes. FRET between PhycoE and Cy5 was measured in intervals of 5-15s. Reaction mixtures contained HOPS complex, Sec17, and variable amounts of Sec18.

Data availability statement

The cryo-EM maps will be deposited at the Electron Microscopy Data Bank (EMDB) and the coordinates will be deposited in the Protein Data Bank. Motion-corrected micrographs will be deposited in the Electron Microscopy Public Image Archive (EMPIAR). The data will be made publicly available as of the date of publication. Original code reported in this paper will be deposited on a publicly available GitHub page. The mass spectroscopy data will be deposited in a publicly available repository.

Acknowledgments

We thank William I. Weis and Joseph D. Puglisi for stimulating discussions. We thank the National Institutes of Mental Health (NIMH) for support (RO1MH63105 to A.T.B., 1F31MH134477 to Y.A.K.). Y.A.K was additionally supported in part by an NSF GRFP and the Knight-Hennessy Scholarship. K.I.W. was supported by a postdoctoral fellowship from the Helen Hay Whitney Foundation, supported by the Howard Hughes Medical Institute. W.T.W. is supported by a grant from the NIH (2R35GM118037). We thank the Vincent Coates Foundation Mass Spectrometry Laboratory, Stanford University Mass Spectrometry (RRID:SCR_017801) for utilizing the Thermo Orbitrap Eclipse nanoLC/MS system (RRID:SCR_022212) that was purchased with funding from the National Institutes of Health Shared Instrumentation Grant 1S10OD030473, the Stanford Cancer Institute Proteomics/Mass Spectrometry Shared Resource (NIH P30 CA124435).

Author contributions

Y.A.K and A.T.B conceived and designed experiments. K.I.W, B.S., and E.M. assisted Y.A.K. with cryo-EM data collection. Y.A.K. performed and analyzed all experimental data. K.I.W. assisted Y.A.K. with cryo-EM data processing and model building. R.A.F. and L.E. assisted with protein purification. G.M., F.L., and T.M. assisted with high-resolution MS proteomics data collection and analysis. K.D. assisted with bulk disassembly assays. U.B.C. collected and assisted with smFRET data. W.T.W. performed and analyzed vacuolar fusion assays. Y.A.K., A.T.B., and K.I.W. wrote the manuscript.

825

826 **References**

827 1. Sutton, R. B., Fasshauer, D., Jahn, R. & Brunger, A. T. Crystal structure of a SNARE
828 complex involved in synaptic exocytosis at 2.4 Å resolution. *Nature* **395**, 347–353 (1998).
829 2. Weber, T. *et al.* SNAREpins: Minimal Machinery for Membrane Fusion. *Cell* **92**, 759–772
830 (1998).
831 3. Zhao, M. *et al.* Mechanistic insights into the recycling machine of the SNARE complex.
832 *Nature* **518**, 61–67 (2015).
833 4. Söllner, T., Bennett, M. K., Whiteheart, S. W., Scheller, R. H. & Rothman, J. E. A protein
834 assembly-disassembly pathway in vitro that may correspond to sequential steps of synaptic
835 vesicle docking, activation, and fusion. *Cell* **75**, 409–418 (1993).
836 5. Jahn, R., Cafiso, D. C. & Tamm, L. K. Mechanisms of SNARE proteins in membrane fusion.
837 *Nat. Rev. Mol. Cell Biol.* 1–18 (2023) doi:10.1038/s41580-023-00668-x.
838 6. White, K. I., Zhao, M., Choi, U. B., Pfuetzner, R. A. & Brunger, A. T. Structural principles of
839 SNARE complex recognition by the AAA+ protein NSF. *eLife* **7**, e38888 (2018).
840 7. Maillard, R. A. *et al.* ClpX(P) Generates Mechanical Force to Unfold and Translocate Its
841 Protein Substrates. *Cell* **145**, 459–469 (2011).
842 8. Wickner, W. & Schekman, R. Membrane fusion. *Nat. Struct. Mol. Biol.* **15**, 658–664 (2008).
843 9. Südhof, T. C. Neurotransmitter Release: The Last Millisecond in the Life of a Synaptic
844 Vesicle. *Neuron* **80**, 675–690 (2013).
845 10. Ungar, D. & Hughson, F. M. SNARE Protein Structure and Function. *Annu. Rev. Cell Dev.*
846 *Biol.* **19**, 493–517 (2003).
847 11. Rizo, J. Molecular Mechanisms Underlying Neurotransmitter Release. *Annu. Rev. Biophys.*
848 **51**, 377–408 (2022).

849 12. Liang, B., Kiessling, V. & Tamm, L. K. Prefusion structure of syntaxin-1A suggests pathway
850 for folding into neuronal trans-SNARE complex fusion intermediate. *Proc. Natl. Acad. Sci.*
851 **110**, 19384–19389 (2013).
852 13. White, K. I., Zhao, M., Choi, U. B., Pfuetzner, R. A. & Brunger, A. T. Structural principles of
853 SNARE complex recognition by the AAA+ protein NSF. *eLife* **7**, e38888 (2018).
854 14. Choi, U. B. *et al.* NSF-mediated disassembly of on- and off-pathway SNARE complexes and
855 inhibition by complexin. *eLife* **7**, e36497 (2018).
856 15. Yoon, T.-Y. & Munson, M. SNARE complex assembly and disassembly. *Curr. Biol.* **28**,
857 R397–R401 (2018).
858 16. Khan, Y. A., White, K. I. & Brunger, A. T. The AAA+ superfamily: a review of the structural
859 and mechanistic principles of these molecular machines. *Crit. Rev. Biochem. Mol. Biol.* **57**,
860 156–187 (2022).
861 17. Hanson, P. I. & Whiteheart, S. W. AAA+ proteins: have engine, will work. *Nat. Rev. Mol. Cell*
862 *Biol.* **6**, 519–529 (2005).
863 18. Puchades, C., Sandate, C. R. & Lander, G. C. The molecular principles governing the
864 activity and functional diversity of AAA+ proteins. *Nat. Rev. Mol. Cell Biol.* **21**, 43–58 (2020).
865 19. Nagiec, E. E., Bernstein, A. & Whiteheart, S. W. Each Domain of the N-Ethylmaleimide-
866 sensitive Fusion Protein Contributes to Its Transport Activity (*). *J. Biol. Chem.* **270**, 29182–
867 29188 (1995).
868 20. Novick, P., Field, C. & Schekman, R. Identification of 23 complementation groups required
869 for post-translational events in the yeast secretory pathway. *Cell* **21**, 205–215 (1980).
870 21. Ma, C., Su, L., Seven, A. B., Xu, Y. & Rizo, J. Reconstitution of the vital functions of Munc18
871 and Munc13 in neurotransmitter release. *Science* **339**, 421–425 (2013).
872 22. Lai, Y. *et al.* Molecular Mechanisms of Synaptic Vesicle Priming by Munc13 and Munc18.
873 *Neuron* **95**, 591-607.e10 (2017).

874 23. Gao, Y. *et al.* Sensory deficit screen identifies nsf mutation that differentially affects SNARE
875 recycling and quality control. *Cell Rep.* **42**, 112345 (2023).
876 24. Leitz, J. *et al.* Beyond the MUN domain, Munc13 controls priming and depriming of synaptic
877 vesicles. *Cell Rep.* **43**, 114026 (2024).
878 25. Ryu, J.-K. *et al.* Spring-loaded unraveling of a single SNARE complex by NSF in one round
879 of ATP turnover. *Science* **347**, 1485–1489 (2015).
880 26. Ryu, J.-K., Jahn, R. & Yoon, T.-Y. Review: Progresses in understanding N-ethylmaleimide
881 sensitive factor (NSF) mediated disassembly of SNARE complexes. *Biopolymers* **105**, 518–
882 531 (2016).
883 27. White, K. I. *et al.* NSF converts syntaxin clusters to a priming-ready state. *Unpublished*.
884 28. Whiteheart, S. W. *et al.* N-ethylmaleimide-sensitive fusion protein: a trimeric ATPase whose
885 hydrolysis of ATP is required for membrane fusion. *J. Cell Biol.* **126**, 945–954 (1994).
886 29. de la Peña, A. H., Goodall, E. A., Gates, S. N., Lander, G. C. & Martin, A. Substrate-
887 engaged 26S proteasome structures reveal mechanisms for ATP-hydrolysis–driven
888 translocation. *Science* **362**, eaav0725 (2018).
889 30. Rizo, A. N. *et al.* Structural basis for substrate gripping and translocation by the ClpB AAA+
890 disaggregase. *Nat. Commun.* **10**, 2393 (2019).
891 31. Fernandez, I. *et al.* Three-dimensional structure of an evolutionarily conserved N-terminal
892 domain of syntaxin 1A. *Cell* **94**, 841–849 (1998).
893 32. DAmico, K. A. *et al.* Structure of a membrane tethering complex incorporating multiple
894 SNAREs. *Nat. Struct. Mol. Biol.* 1–9 (2024) doi:10.1038/s41594-023-01164-8.
895 33. Wang, T., Li, L. & Hong, W. SNARE proteins in membrane trafficking. *Traffic* **18**, 767–775
896 (2017).
897 34. Baryshnikova, A. Systematic Functional Annotation and Visualization of Biological
898 Networks. *Cell Syst.* **2**, 412–421 (2016).

899 35. Thomas, P. D. *et al.* PANTHER: Making genome-scale phylogenetics accessible to all.
900 *Protein Sci.* **31**, 8–22 (2022).
901 36. Kato, M. & Wickner, W. Ergosterol is required for the Sec18/ATP-dependent priming step of
902 homotypic vacuole fusion. *EMBO J.* **20**, 4035–4040 (2001).
903 37. Ungermann, C., Wickner, W. & Xu, Z. Vacuole acidification is required for trans-SNARE
904 pairing, LMA1 release, and homotypic fusion. *Proc. Natl. Acad. Sci.* **96**, 11194–11199
905 (1999).
906 38. Baker, T. A. & Sauer, R. T. ClpXP, an ATP-powered unfolding and protein-degradation
907 machine. *Biochim. Biophys. Acta BBA - Mol. Cell Res.* **1823**, 15–28 (2012).
908 39. Merkley, E. D. *et al.* Distance restraints from crosslinking mass spectrometry: Mining a
909 molecular dynamics simulation database to evaluate lysine–lysine distances. *Protein Sci.*
910 *Publ. Protein Soc.* **23**, 747–759 (2014).
911 40. Chin, J. W. *et al.* Addition of p-Azido-l-phenylalanine to the Genetic Code of Escherichia
912 coli. *J. Am. Chem. Soc.* **124**, 9026–9027 (2002).
913 41. Punjani, A. & Fleet, D. J. 3D variability analysis: Resolving continuous flexibility and discrete
914 heterogeneity from single particle cryo-EM. *J. Struct. Biol.* **213**, 107702 (2021).
915 42. Zucchi, P. C. & Zick, M. Membrane fusion catalyzed by a Rab, SNAREs, and SNARE
916 chaperones is accompanied by enhanced permeability to small molecules and by lysis. *Mol.*
917 *Biol. Cell* **22**, 4635–4646 (2011).
918 43. Zick, M., Stroupe, C., Orr, A., Douville, D. & Wickner, W. T. Membranes linked by trans-
919 SNARE complexes require lipids prone to non-bilayer structure for progression to fusion.
920 *eLife* **3**, e01879.
921 44. Shein, M. *et al.* Characterizing ATP processing by the AAA+ protein p97 at the atomic level.
922 *Nat. Chem.* **16**, 363–372 (2024).
923 45. Shvarev, D. *et al.* Structure of the HOPS tethering complex, a lysosomal membrane fusion
924 machinery. *eLife* **11**, e80901 (2022).

46. Song, H., Orr, A. S., Lee, M., Harner, M. E. & Wickner, W. T. HOPS recognizes each SNARE, assembling ternary trans-complexes for rapid fusion upon engagement with the 4th SNARE. *eLife* **9**, e53559 (2020).

47. Song, H., Torng, T. L., Orr, A. S., Brunger, A. T. & Wickner, W. T. Sec17/Sec18 can support membrane fusion without help from completion of SNARE zippering. *eLife* https://elifesciences.org/articles/67578 (2021) doi:10.7554/eLife.67578.

48. Orr, A. & Wickner, W. Sec18 supports membrane fusion by promoting Sec17 membrane association. *Mol. Biol. Cell* **33**, ar127 (2022).

49. Kelch, B. A., Makino, D. L., O'Donnell, M. & Kuriyan, J. Clamp loader ATPases and the evolution of DNA replication machinery. *BMC Biol.* **10**, 34 (2012).

50. Verma, A. R., Ray, K. K., Bodick, M., Kinz-Thompson, C. D. & Gonzalez, R. L. Increasing the accuracy of single-molecule data analysis using tMAVEN. *Biophys. J.* (2024) doi:10.1016/j.bpj.2024.01.022.

51. Scheres, S. H. W. A Bayesian view on cryo-EM structure determination. *J. Mol. Biol.* **415**, 406–418 (2012).

52. cryoSPARC: algorithms for rapid unsupervised cryo-EM structure determination - PubMed. https://pubmed.ncbi.nlm.nih.gov/28165473/.

53. Jumper, J. *et al.* Highly accurate protein structure prediction with AlphaFold. *Nature* **596**, 583–589 (2021).

54. Emsley, P. & Cowtan, K. Coot: model-building tools for molecular graphics. *Acta Crystallogr. D Biol. Crystallogr.* **60**, 2126–2132 (2004).

55. Adams, P. D. *et al.* The Phenix Software for Automated Determination of Macromolecular Structures. *Methods San Diego Calif* **55**, 94–106 (2011).

56. Croll, T. I. ISOLDE: a physically realistic environment for model building into low-resolution electron-density maps. *Acta Crystallogr. Sect. Struct. Biol.* **74**, 519–530 (2018).

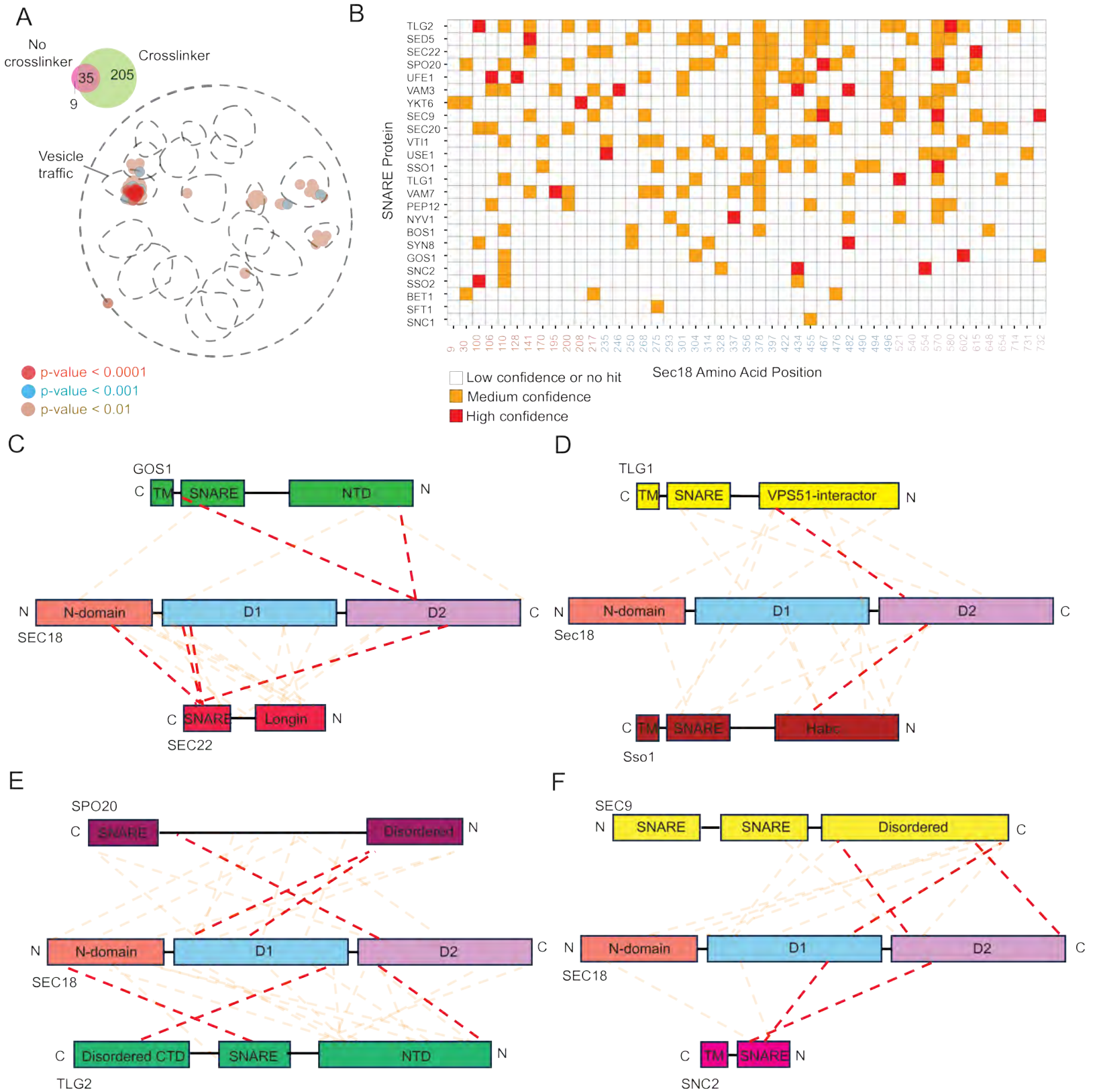
A
No crosslinker
Crosslinker
35
205
9
Vesicle traffic
p-value < 0.0001
p-value < 0.001
p-value < 0.01
B
SNARE Protein
TLG2
SED5
SEC22
SPO20
UFE1
VAM3
YKT6
SEC9
SEC20
VTI1
USE1
SSO1
TLG1
VAM7
PEP12
NYV1
BOS1
SYN8
GOS1
SNC2
SSO2
BET1
SFT1
SNC1
Sec18 Amino Acid Position
Low confidence or no hit
Medium confidence
High confidence
C
GOS1
TM
SNARE
NTD
N-domain
D1
D2
SEC18
SNARE
Longin
SEC22
D
TLG1
TM
SNARE
VPS51-interactor
N-domain
D1
D2
Sec18
TM
SNARE
Habc
Sso1
E
SPO20
SNARE
Disordered
N-domain
D1
D2
SEC18
Disordered CTD
SNARE
NTD
TLG2
F
SEC9
SNARE
SNARE
Disordered
N-domain
D1
D2
SEC18
TM
SNARE
SNC2

Figure 1

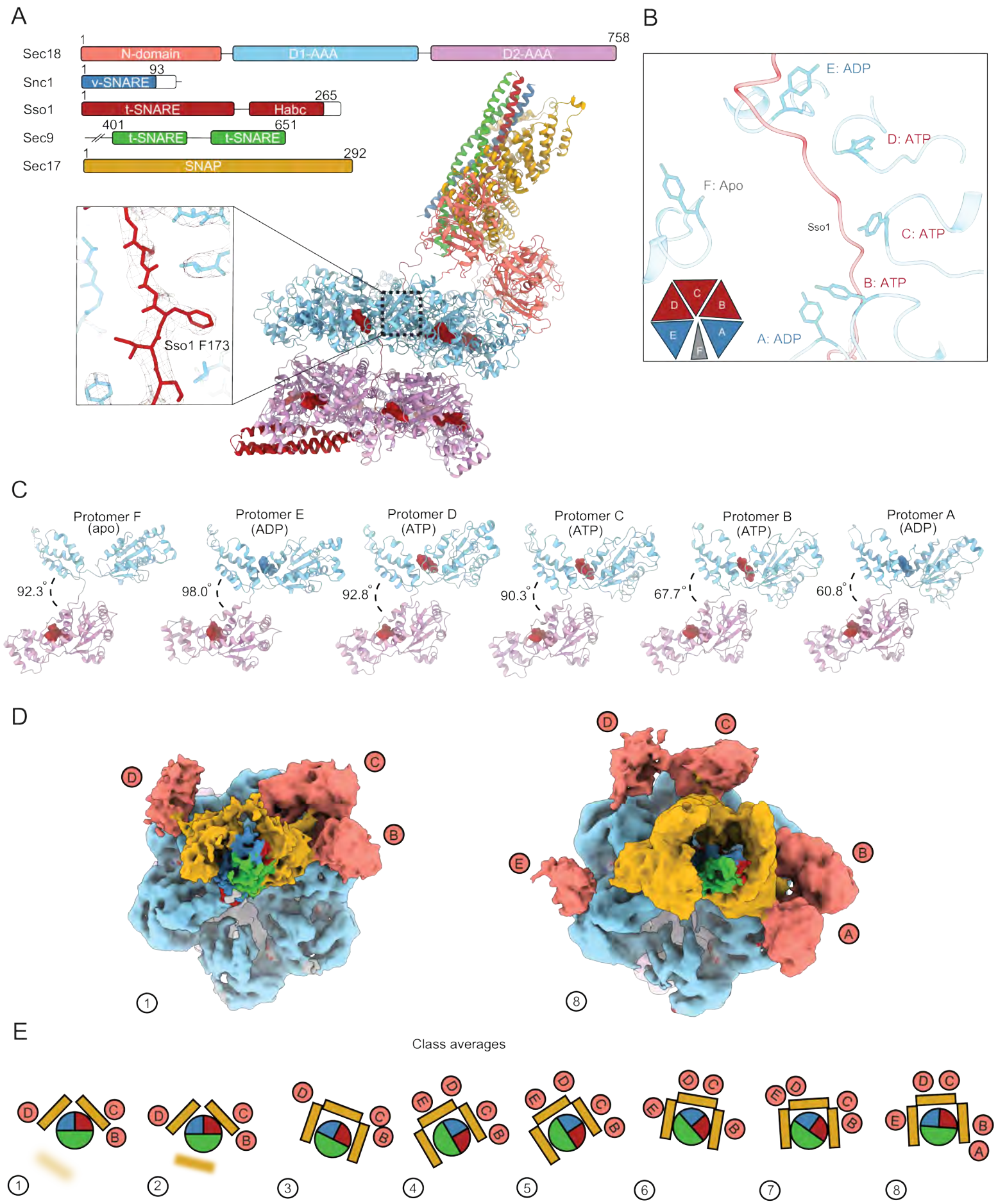
A
Sec18
N-domain
D1-AAA
D2-AAA
1
758
Snc1
v-SNARE
1
93
Sso1
t-SNARE
Habc
1
265
Sec9
t-SNARE
t-SNARE
401
651
Sec17
SNAP
1
292
Sso1 F173
B
E: ADP
D: ATP
F: Apo
Sso1
C: ATP
B: ATP
A: ADP
C
Protomer F (apo)
Protomer E (ADP)
Protomer D (ATP)
Protomer C (ATP)
Protomer B (ATP)
Protomer A (ADP)
92.3°
98.0°
92.8°
90.3°
67.7°
60.8°
D
1
8
E
Class averages
1
2
3
4
5
6
7
8

Figure 2

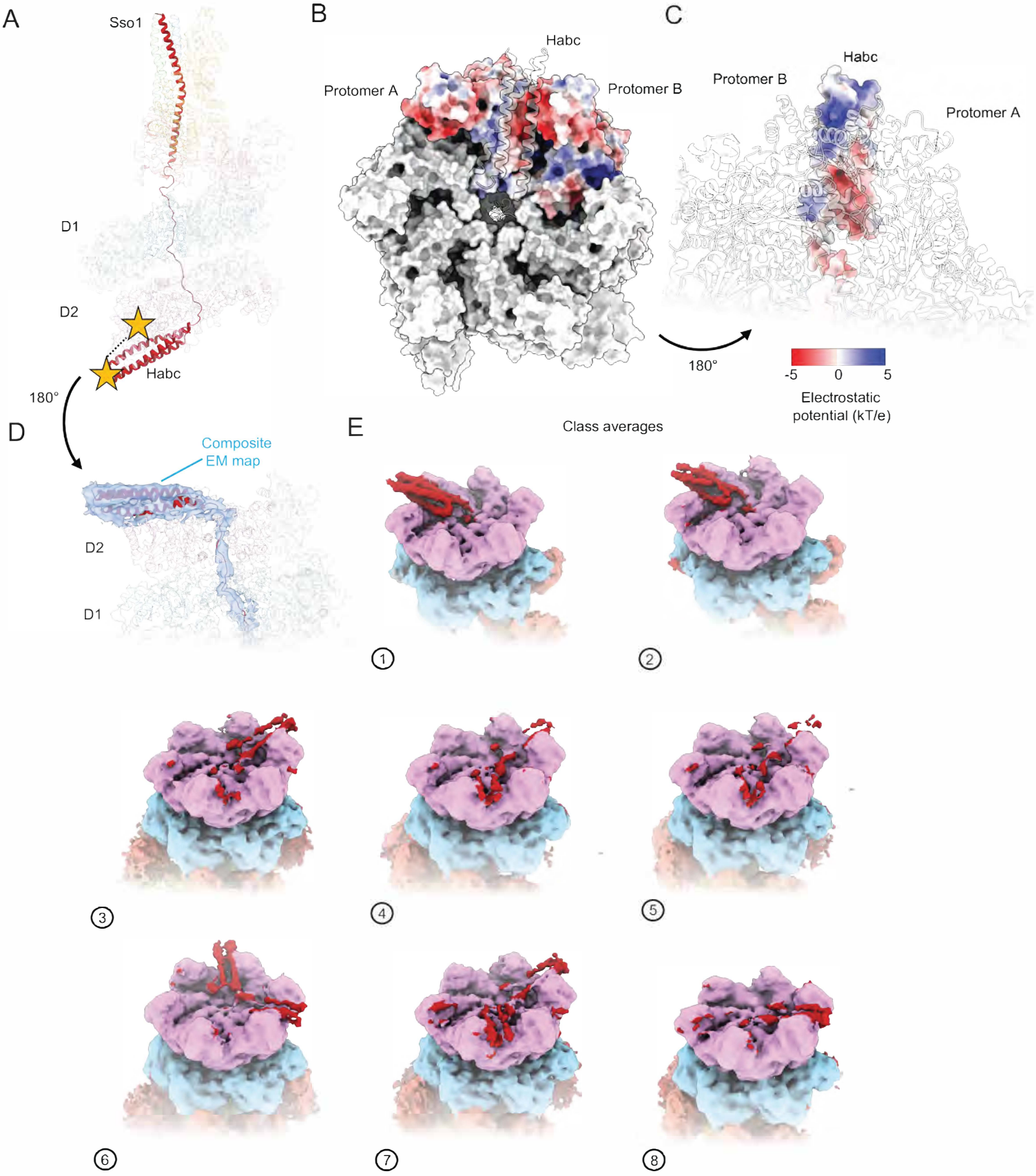
A
Sso1
D1
D2
Habc
180°
B
Habc
Protomer A
Protomer B
C
Habc
Protomer B
Protomer A
180°
-5
0
5
Electrostatic potential (kT/e)
D
Composite EM map
D2
D1
E
Class averages
1
2
3
4
5
6
7
8

Figure 3

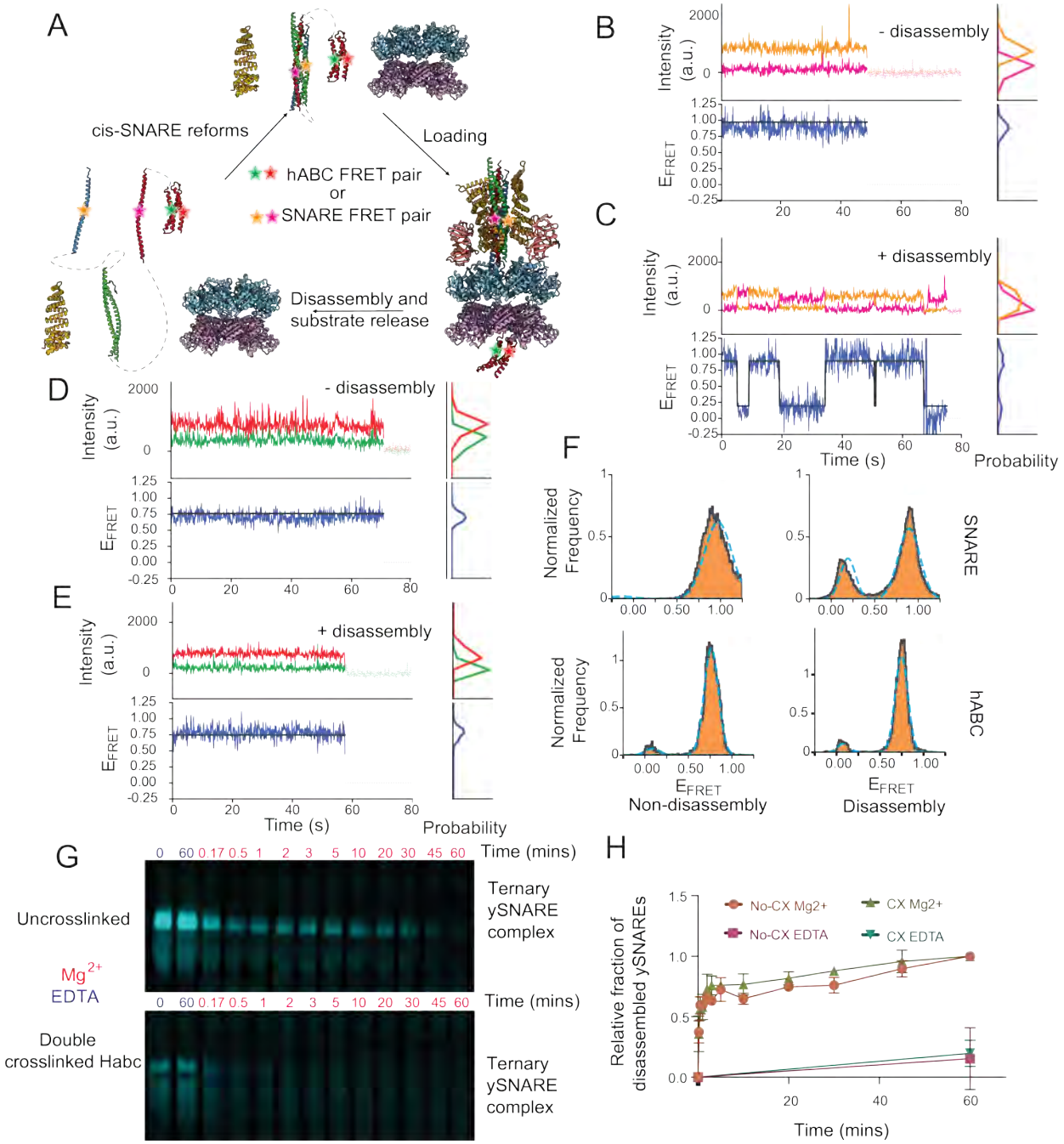
A
cis-SNARE reforms
Loading
hABC FRET pair
or
SNARE FRET pair
Disassembly and
substrate release
B
- disassembly
Intensity (a.u.)
E_{FRET}
C
+ disassembly
Time (s)
Probability
D
- disassembly
E
+ disassembly
F
Normalized Frequency
SNARE
hABC
E_{FRET}
Non-disassembly
Disassembly
G
Time (mins)
Uncrosslinked
Mg^{2+}
EDTA
Ternary ySNARE complex
Double crosslinked Habc
H
No-CX Mg2+
CX Mg2+
No-CX EDTA
CX EDTA
Relative fraction of disassembled ySNAREs
Time (mins)

Figure 4

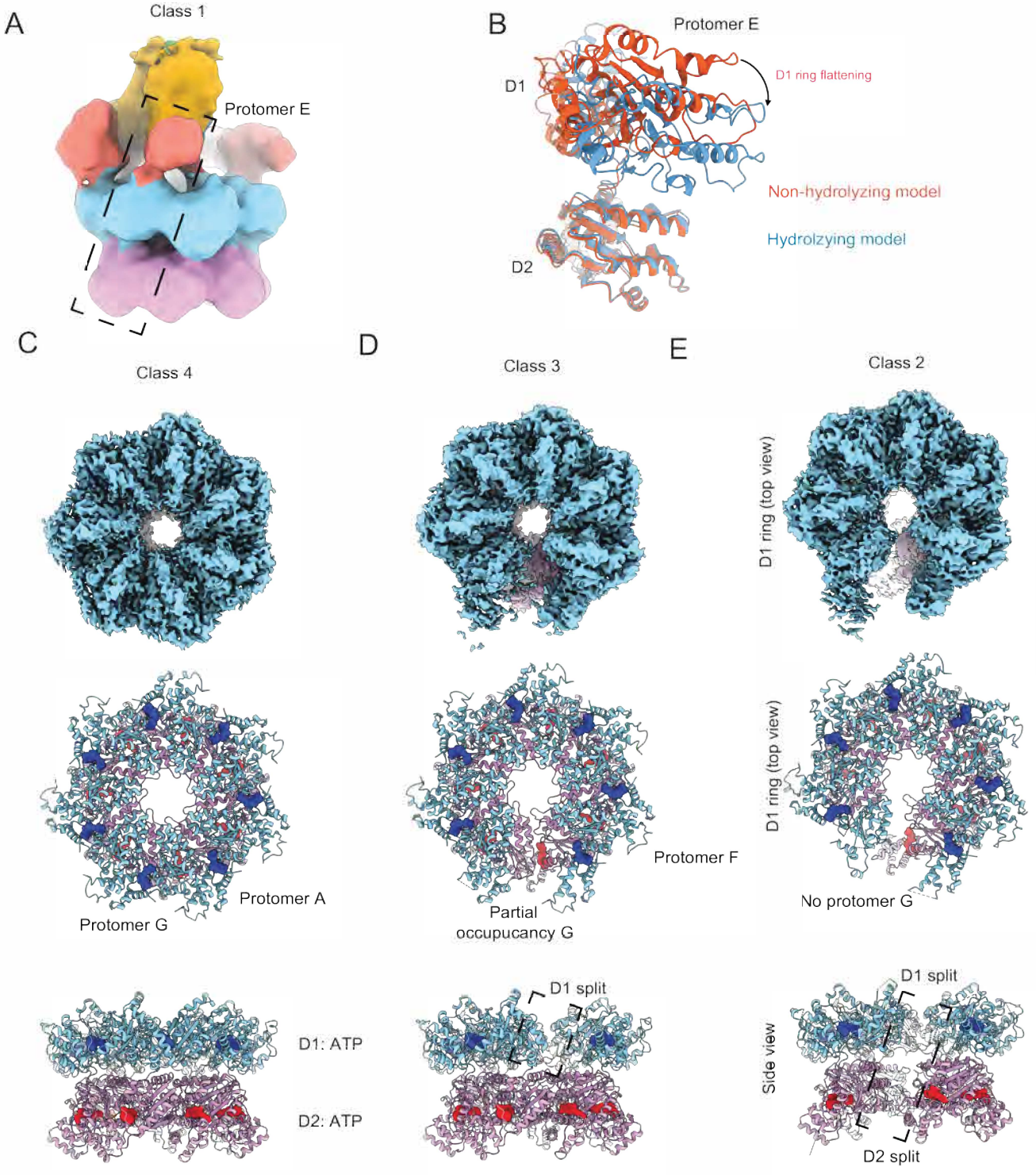
A
Class 1
Protomer E
B
Protomer E
D1
D1 ring flattening
Non-hydrolyzing model
Hydrolzying model
D2
C
Class 4
Protomer A
Protomer G
D1: ATP
D2: ATP
D
Class 3
Protomer F
Partial
occupucancy G
D1 split
E
Class 2
D1 ring (top view)
D1 ring (top view)
No protomer G
D1 split
Side view
D2 split

Figure 5

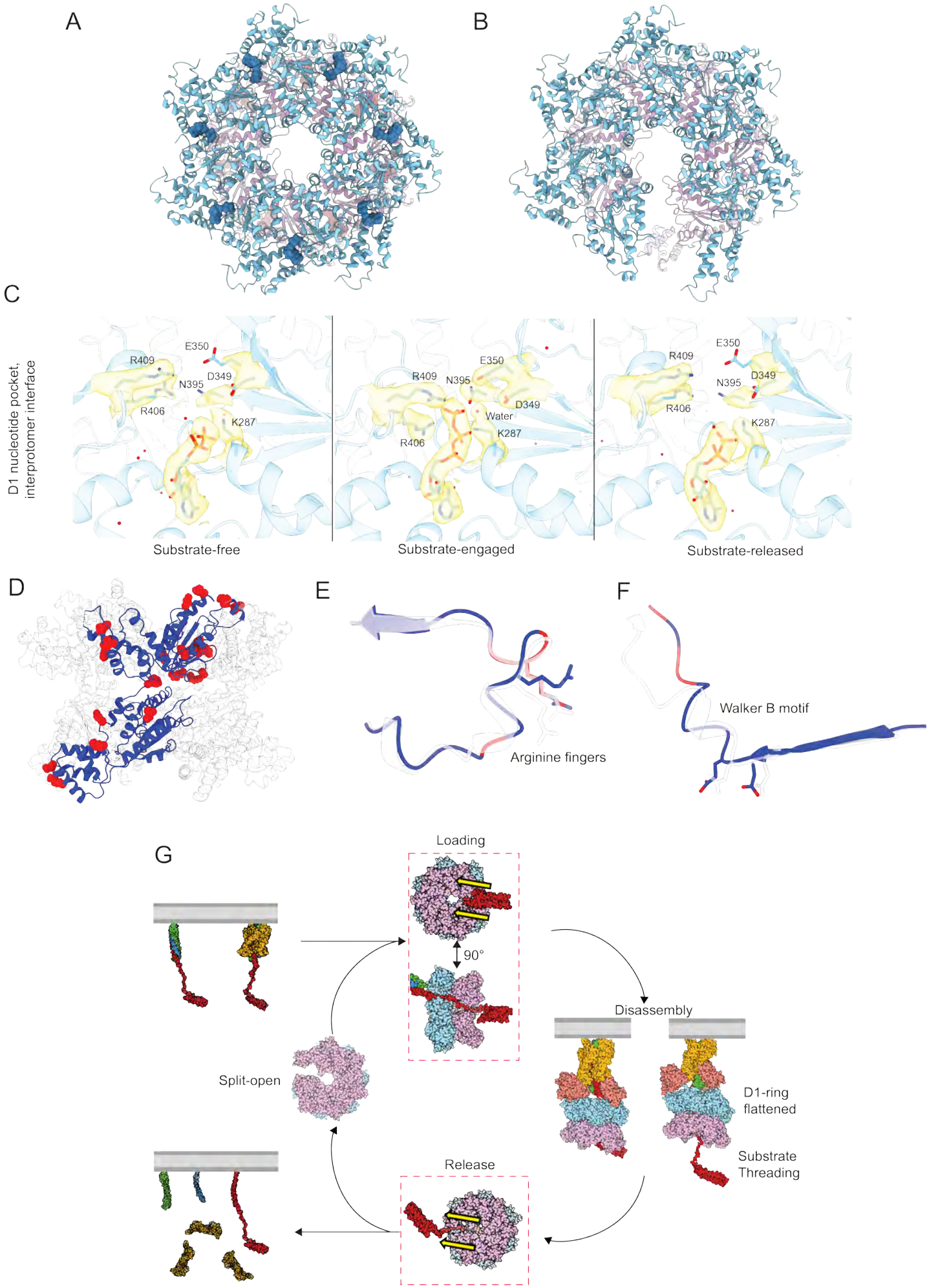
A
B
C
D1 nucleotide pocket, interprotomer interface
E350
R409
D349
N395
R406
K287
Water
Substrate-free
Substrate-engaged
Substrate-released
D
E
Arginine fingers
F
Walker B motif
G
Loading
90°
Disassembly
D1-ring flattened
Substrate Threading
Release
Split-open

Figure 6

Extended Data Table 1 | Cryo-EM data collection, refinement, and validation statistics

	Y20S, non-hydrolyzing condition									Y20S, hydrolyzing condition				Sec18, hydrolyzing condition		NSF, hydrolyzing condition	
	#1 Class 1 (EMDB-) (PDB)	#2 Class 2 (EMDB-) (PDB)	#3 Class 3 (EMDB-) (PDB)	#4 Class 4 (EMDB-) (PDB)	#5 Class 5 (EMDB-) (PDB)	#6 Class 6 (EMDB-) (PDB)	#7 Class 7 (EMDB-) (PDB)	#8 Class 8 (EMDB-) (PDB)	#9 All Merge D1/D2 (EMDB-) (PDB)	#10 Class 1 (no model deposited)	#11 Class 2 (EMDB-) (PDB)	#12 Class 3 (EMDB-) (PDB)	#13 Class 4 (EMDB-) (PDB)	#14 Class 1 (EMDB-) (PDB)	#15 Class 2 (EMDB-) (PDB)	#16 Class 1 (EMDB-) (PDB)	#17 Class 2 (EMDB-) (PDB)
Data collection and processing																	
Magnification	130,000×	130,000×	130,000×	130,000×	130,000×	130,000×	130,000×	130,000×	130,000x	130,000x	130,000x	130,000x	130,000x	130,000x	130,000x	130,000x	130,000x
Camera	Gatan K3	Gatan K3	Gatan K3	Gatan K3	Gatan K3	Gatan K3	Gatan K3	Gatan K3	Gatan K3	Falcon 4i	Falcon 4i	Falcon 4i	Falcon 4i	Gatan K3	Gatan K3	Gatan K3	Gatan K3
Voltage (kV)	300	300	300	300	300	300	300	300	300	300	300	300	300	300	300	300	300
Electron exposure (e–/Å^2)	26.8	26.8	26.8	26.8	26.8	26.8	26.8	26.8	26.8	51.48	51.48	51.48	51.48	25.5	25.5	39.04	39.04
Defocus range (μm)	-1.0 to -2.0	-1.0 to -2.0	-1.0 to -2.0	-1.0 to -2.0	-1.0 to -2.0	-1.0 to -2.0	-1.0 to -2.0	-1.0 to -2.0	-1.0 to -2.0	-1.0 to -2.0	-1.0 to -2.0	-1.0 to -2.0	-1.0 to -2.0	-1.0 to -2.0	-1.0 to -2.0	-1.0 to -2.0	-1.0 to -2.0
Pixel size (Å, super-res)	0.548	0.548	0.548	0.548	0.548	0.548	0.548	0.548	0.548	0.49	0.49	0.49	0.49	0.548	0.548	0.548	0.548
Exposure time (seconds)	4	4	4	4	4	4	4	4	4	6.93	6.93	6.93	6.93	4	4	4	4
Number of frames per exposure	80	80	80	80	80	80	80	80	80	2133 (EER fractionation of 42)	2133 (EER fractionation of 42)	2133 (EER fractionation of 42)	2133 (EER fractionation of 42)	80	80	80	80
Number of movies	12,439	12,439	12,439	12,439	12,439	12,439	12,439	12,439	12,439	14455	14455	14455	14455	7821	7821	13375	13375
Symmetry imposed	C1	C1	C1	C1	C1	C1	C1	C1	C1	C1	C1	C1	C1	C1	C1	C1	C1
Final particle images (no.)	41,159	35,723	79,060	26,603	33,084	64,857	69,608	31,497	381,591	6,356	86,542	91,962	96,291	280,935	16,074	72,069	11,844
Map resolution (Å)	3.89	3.91	3.73	4.61	4.29	3.73	3.75	4.13	3.4	10.88	3.38	3.36	3.18	2.99	6.09	3.60	4.70
FSC threshold	0.143	0.143	0.143	0.143	0.143	0.143	0.143	0.143	0.143	0.143	0.143	0.143	0.143	0.143	0.143	0.143	0.143
Model information																	
Initial model used (PDB code)	3B5N, Sec17/18 from AlphaFold2	3B5N, Sec17/18 from AlphaFold2	3B5N, Sec17/18 from AlphaFold2	3B5N, Sec17/18 from AlphaFold2	3B5N, Sec17/18 from AlphaFold2	3B5N, Sec17/18 from AlphaFold2	3B5N, Sec17/18 from AlphaFold2	3B5N, Sec17/18 from AlphaFold2	Sec18 from AlphaFold2	Y20S EDTA Class 1	*De novo*	*De novo*	*De novo*	*De novo*	*De novo*	3J94	3J94
Bond RMSD (Å)	0.12	0.012	0.007	0.007	0.010	0.005	0.005	0.010	0.006	No model deposited	0.004	0.013	0.007	0.007	0.006	0.006	0.007
Angle RMSD (°)	1.461	1.473	1.186	1.168	1.206	1.023	1.027	1.243	0.920	No model deposited	1.203	1.444	1.186	1.160	1.090	0.715	1.313
Molprobity score	1.68	1.79	1.58	1.79	1.72	1.73	1.62	1.76	1.55	No model deposited	1.23	1.78	1.78	1.51	1.80	2.00	1.72
Clashscore, all atoms	5.77	8.55	5.80	8.26	8.37	9.22	6.68	7.71	4.01	No model deposited	2.67	8.27	4.49	4.52	9.44	5.37	9.81
Ramachandran. Favored/Allowed/Disfacored (%)	94.77 4.85 0.38	95.35 4.49 0.16	96.15 3.75 0.10	95.12 4.54 0.34	96.11 3.69 0.20	96.41 3.45 0.14	96.24 3.67 0.08	95.81 3.88 0.31	94.80 5.01 0.19	No model deposited	96.95 2.92 0.14	95.16 4.65 0.18	95.13 4.58 0.29	95.95 4.05 0.00	95.73 4.17 0.00	95.64 4.36 0.00	97.17 2.26 0.57
Rotamer outliers (%)	0.61	0.44	0.43	0.69	0.88	0.55	0.52	1.14	0.55	No model deposited	0.08	0.00	1.96	0.93	0.97	3.45	1.19
Cβ outliers (%)	0.02	0.04	0.00	0.04	0.02	0.02	0.00	0.02	0.00	No model deposited	0.04	0.10	0.00	0.00	0.00	0.00	0.00
CaBLAM outliers (%)	2.36	2.08	2.06	2.22	2.09	1.99	2.15	2.14	3.06	No model deposited	0.93	1.36	1.20	0.99	0.99	1.44	1.46

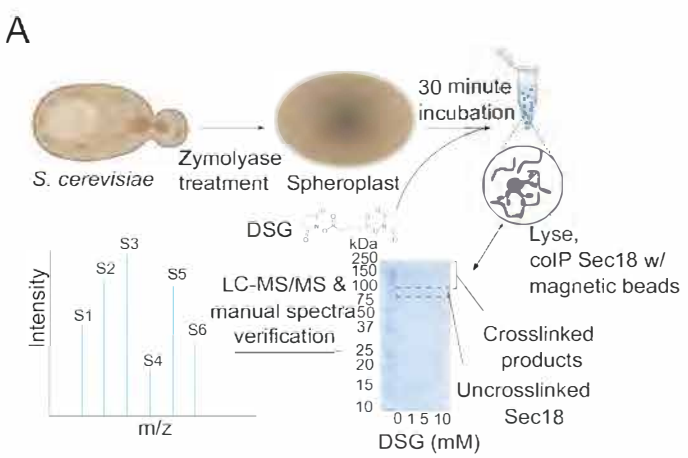

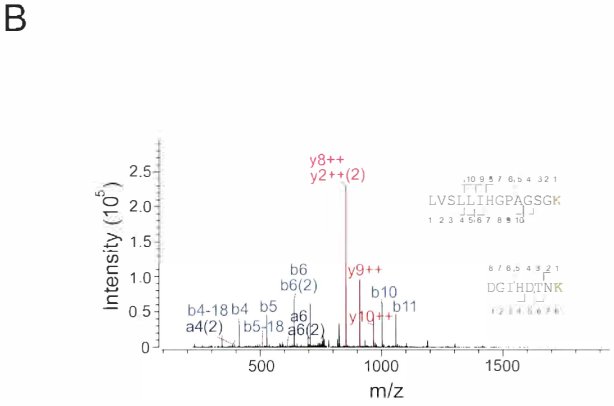

Extended Data Figure 1

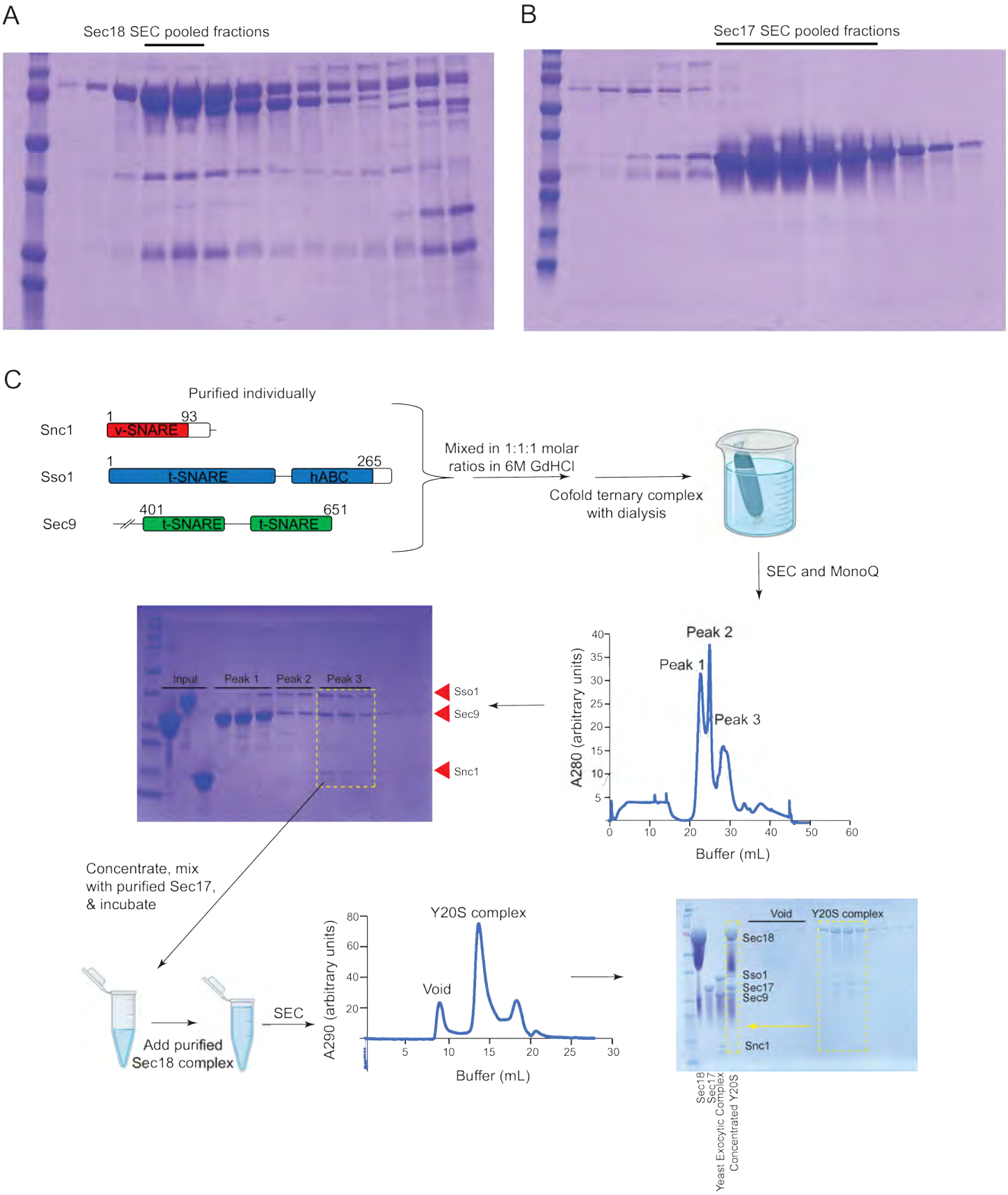

Extended Data Figure 2

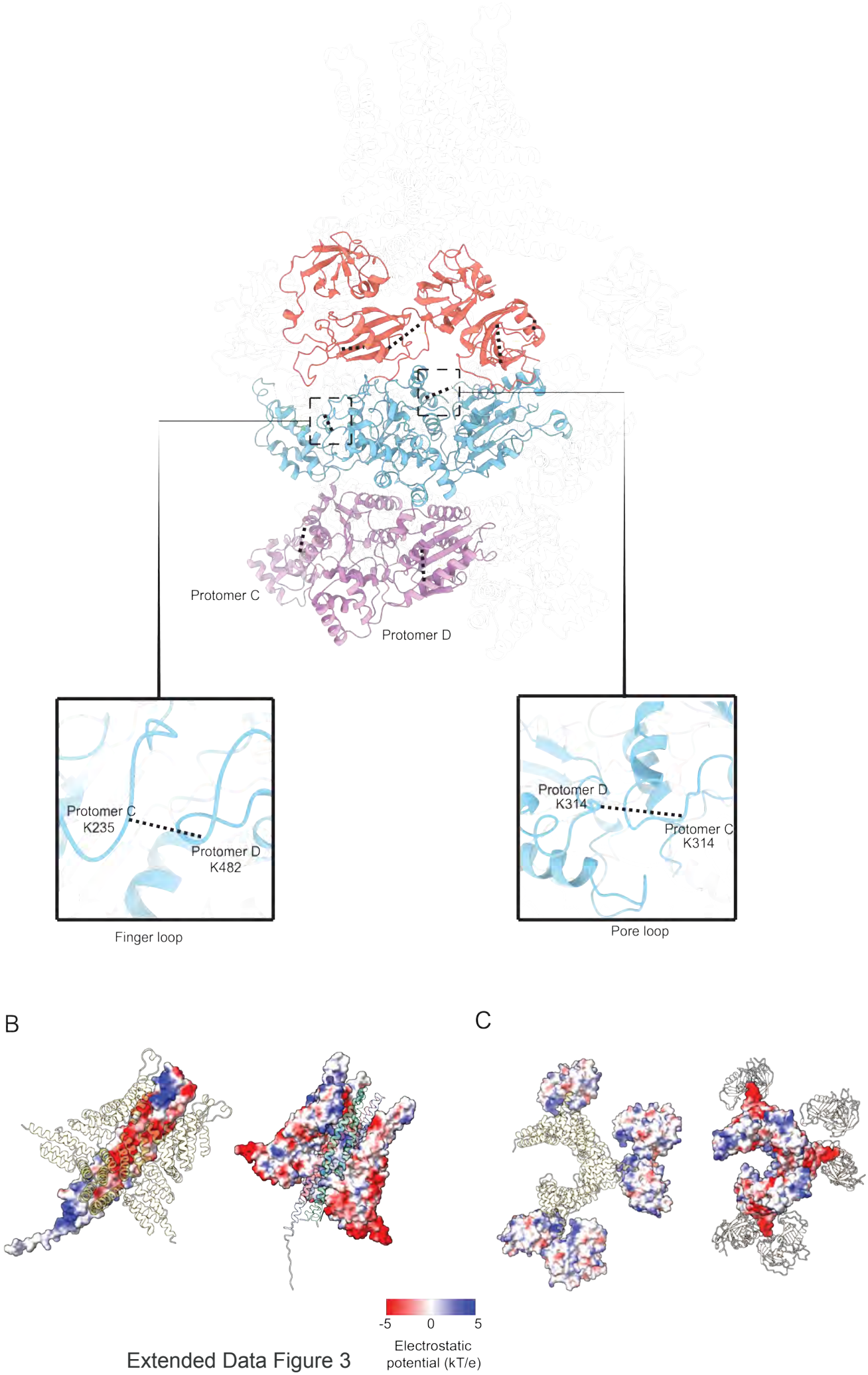

Extended Data Figure 3

A

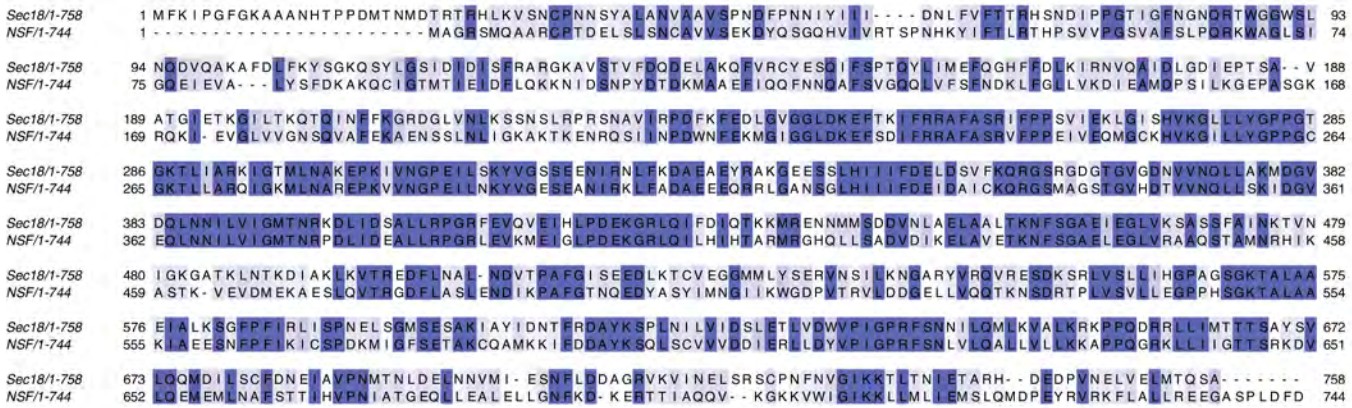

B

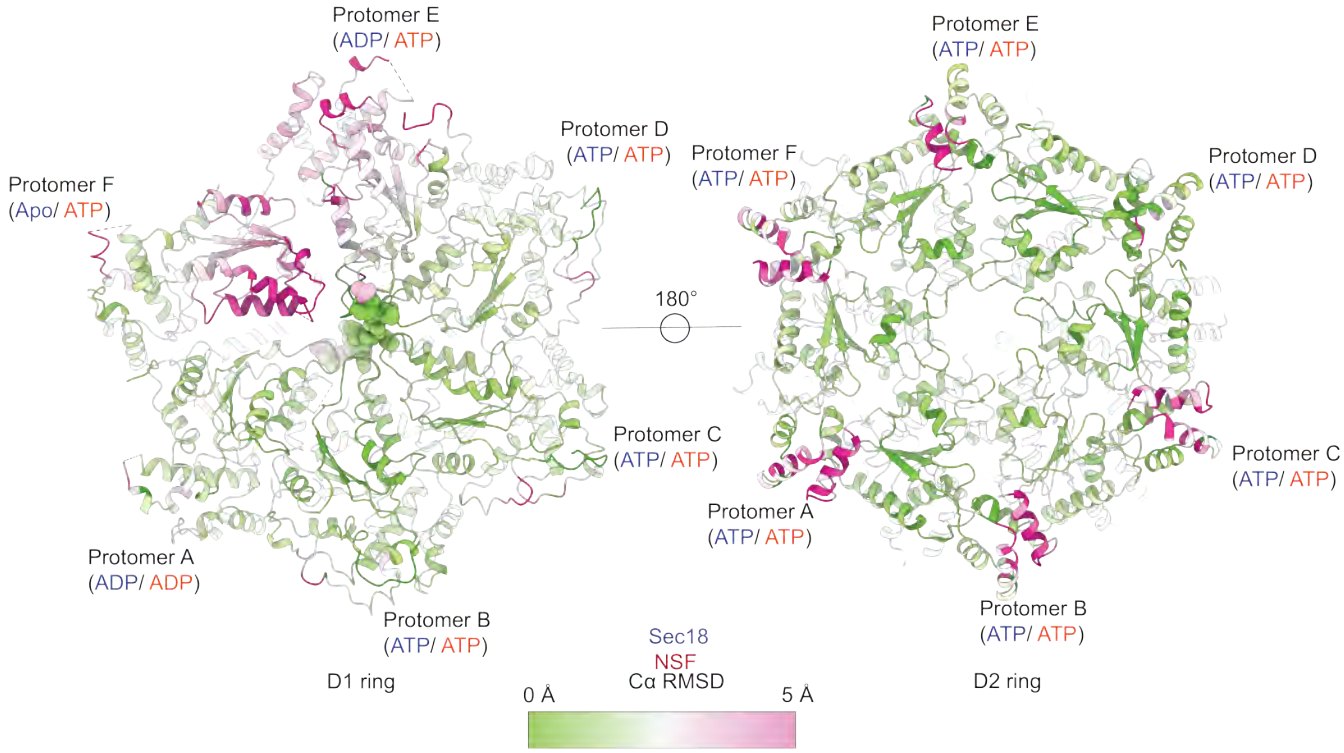

C

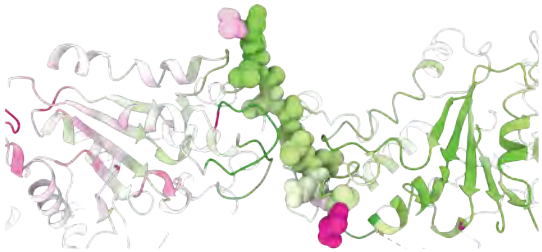

Extended Data Figure 4

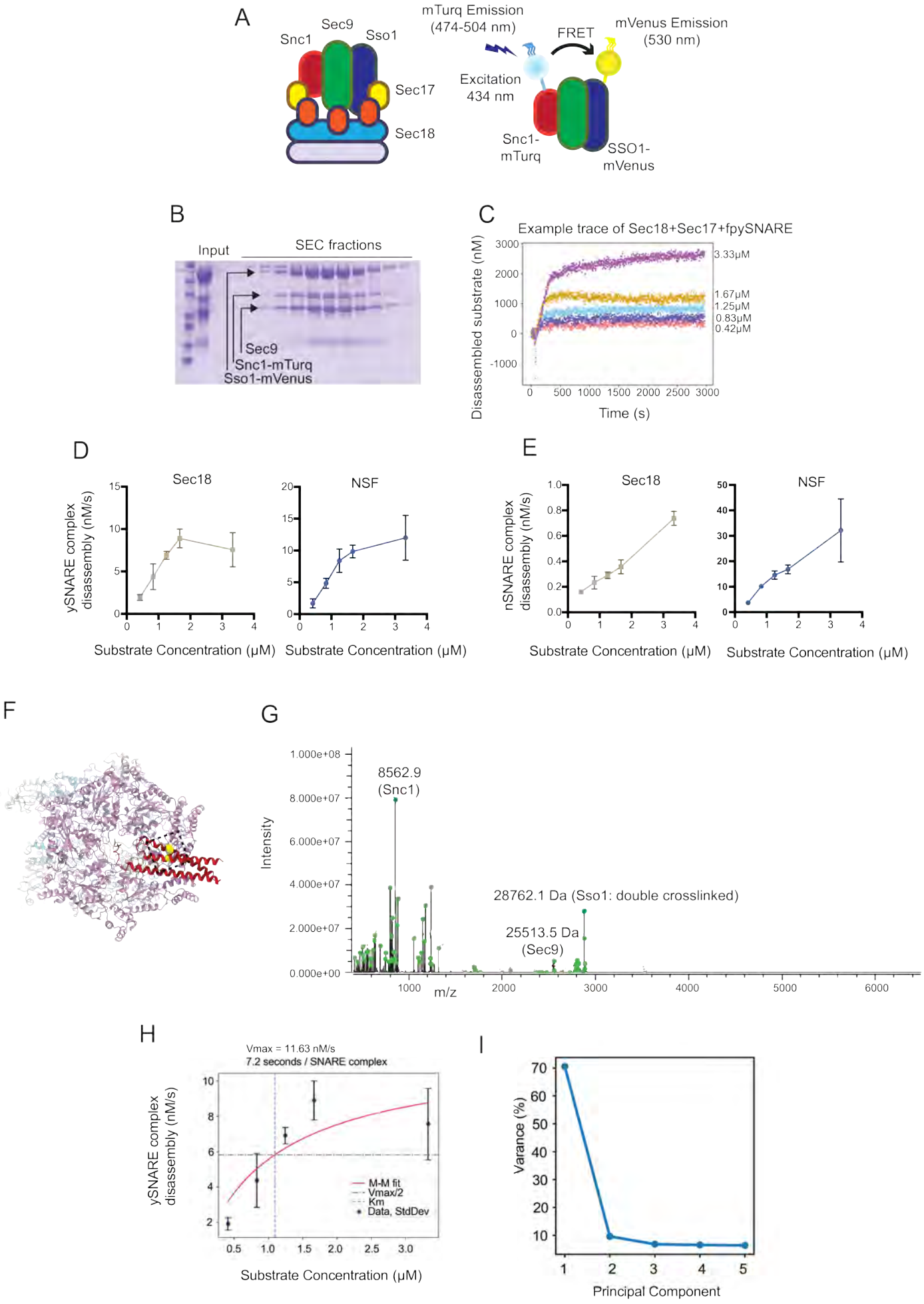

Extended Data Figure 5

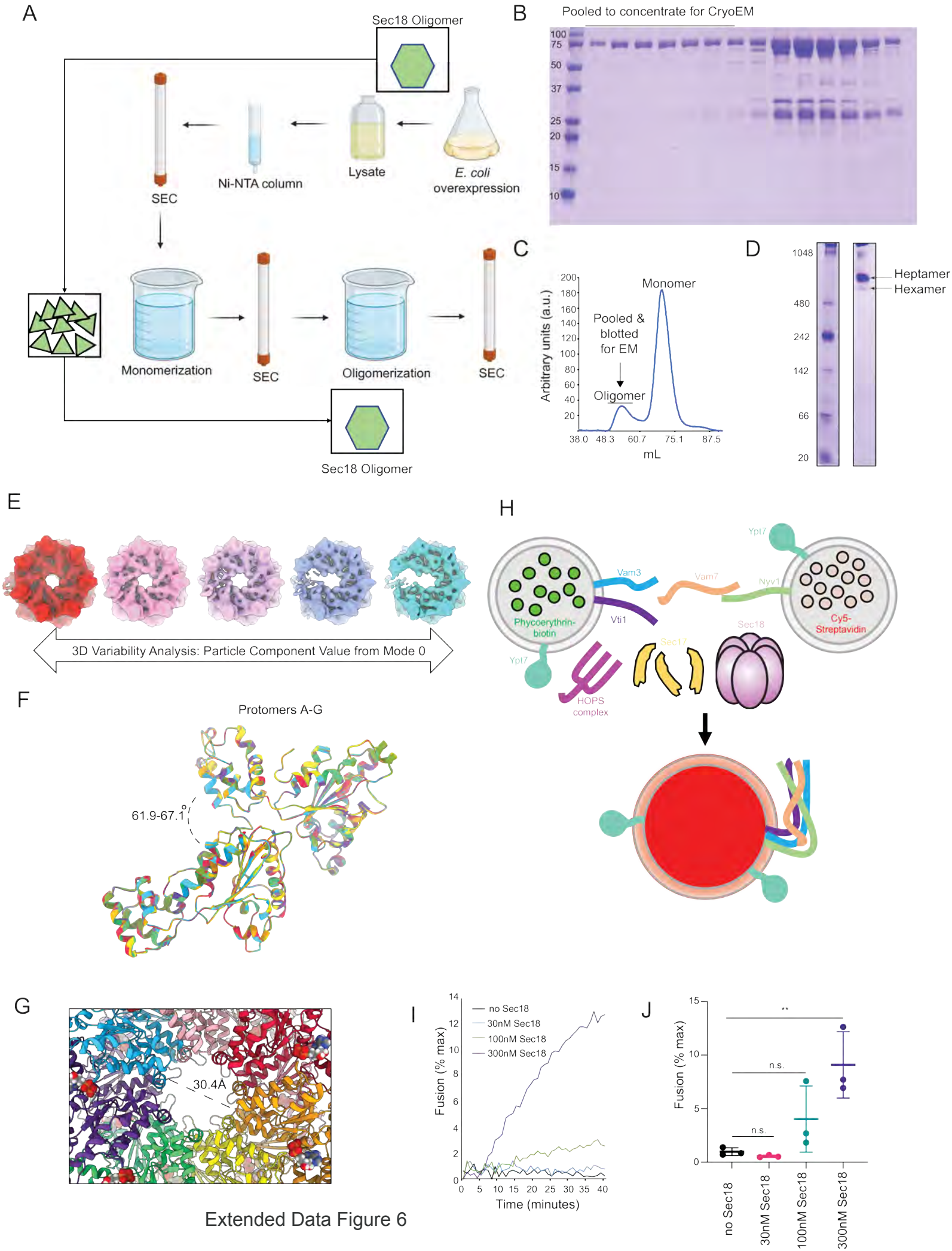

Extended Data Figure 6

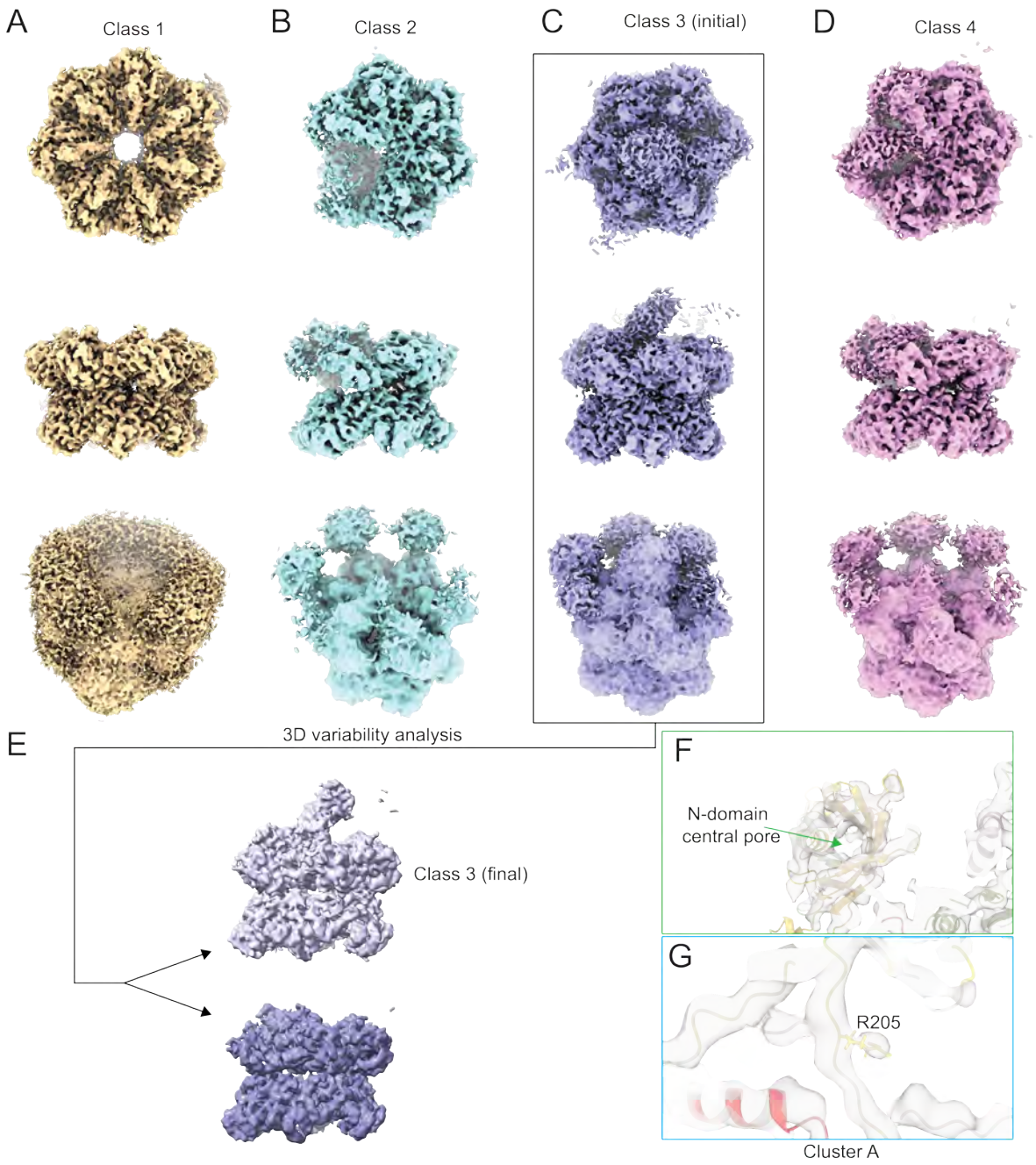

Extended Data Figure 7